

# UCLA

## UCLA Previously Published Works

### Title

Microglia Drive Pockets of Neuroinflammation in Middle Age.

### Permalink

<https://escholarship.org/uc/item/36k8s168>

### Journal

Journal of Neuroscience, 42(19)

### ISSN

0270-6474

### Authors

Moca, Eric N

Lecca, Daniela

Hope, Keenan T

et al.

### Publication Date

2022-05-11

### DOI

10.1523/jneurosci.1922-21.2022



### Copyright Information

This work is made available under the terms of a Creative Commons Attribution-NonCommercial-ShareAlike License, available at

<https://creativecommons.org/licenses/by-nc-sa/4.0/>

Peer reviewed

# Microglia Drive Pockets of Neuroinflammation in Middle Age

Eric N. Moca,<sup>1\*</sup> Daniela Lecca,<sup>2\*</sup> Keenan T. Hope,<sup>1\*</sup>  Fanny Etienne,<sup>1</sup> Ari W. Schaler,<sup>1</sup> Katherine Espinoza,<sup>1</sup> Megan S. Chappell,<sup>1</sup> Daniel T. Gray,<sup>1</sup> David Tweedie,<sup>2</sup> Shanaya Sidhu,<sup>1</sup> Lindsay Masukawa,<sup>1</sup> Hannah Sitoy,<sup>1</sup> Rose Mathew,<sup>3</sup> Daniel R. Saban,<sup>3</sup> Nigel H. Greig,<sup>2</sup> and  Lindsay M. De Biase<sup>1</sup>

<sup>1</sup>Department of Physiology, David Geffen School of Medicine at UCLA, Los Angeles, California 90095, <sup>2</sup>Intramural Research Program, National Institute on Aging, Baltimore, Maryland 21224, and <sup>3</sup>Department of Ophthalmology, Duke University School of Medicine, Durham, North Carolina 27710

During aging, microglia produce inflammatory factors, show reduced tissue surveillance, altered interactions with synapses, and prolonged responses to CNS insults, positioning these cells to have profound impact on the function of nearby neurons. We and others recently showed that microglial attributes differ significantly across brain regions in young adult mice. However, the degree to which microglial properties vary during aging is largely unexplored. Here, we analyze and manipulate microglial aging within the basal ganglia, brain circuits that exhibit prominent regional microglial heterogeneity and where neurons are vulnerable to functional decline and neurodegenerative disease. In male and female mice, we demonstrate that VTA and SNc microglia exhibit unique and premature responses to aging, compared with cortex and NAc microglia. This is associated with localized VTA/SNc neuroinflammation that may compromise synaptic function as early as middle age. Surprisingly, systemic inflammation, local neuron death, and astrocyte aging do not appear to underlie these early aging responses of VTA and SNc microglia. Instead, we found that microglial lysosome status was tightly linked to early aging of VTA microglia. Microglial ablation/repopulation normalized VTA microglial lysosome swelling and suppressed increases in VTA microglial density during aging. In contrast, CX3CR1 receptor KO exacerbated VTA microglial lysosome rearrangements and VTA microglial proliferation during aging. Our findings reveal a previously unappreciated regional variation in onset and magnitude of microglial proliferation and inflammatory factor production during aging and highlight critical links between microglial lysosome status and local microglial responses to aging.

**Key words:** aging; basal ganglia; dopamine neuron; inflammation; lysosome; microglia

## Significance Statement

Microglia are CNS cells that are equipped to regulate neuronal health and function throughout the lifespan. We reveal that microglia in select brain regions begin to proliferate and produce inflammatory factors in late middle age, months before microglia in other brain regions. These findings demonstrate that CNS neuroinflammation during aging is not uniform. Moreover, they raise the possibility that local microglial responses to aging play a critical role in determining which populations of neurons are most vulnerable to functional decline and neurodegenerative disease.

Received Sep. 22, 2021; revised Feb. 18, 2022; accepted Mar. 14, 2022.

Author contributions: E.N.M., D.L., K.T.H., F.E., A.W.S., K.E., M.S.C., D.T.G., D.R.S., N.H.G., and L.M.D. designed research; E.N.M., D.L., K.T.H., F.E., A.W.S., K.E., M.S.C., D.T.G., D.T., S.S., L.M., H.S., R.M., and L.M.D. performed research; E.N.M., D.L., K.T.H., F.E., A.W.S., K.E., M.S.C., D.T.G., D.T., S.S., L.M., H.S., and L.M.D. analyzed data; E.N.M., D.L., K.T.H., F.E., A.W.S., K.E., M.S.C., D.T.G., D.R.S., N.H.G., and L.M.D. edited the paper; L.M.D. wrote the first draft of the paper; L.M.D. wrote the paper.

This work was supported by National Institute on Drug Abuse Intramural Research Program to L.M.D.; National Institute on Aging Intramural Research Program to N.H.G.; David Geffen School of Medicine at UCLA start-up funds to L.M.D.; and Glenn Foundation for Medical Research and American Federation for Aging Research Grant for Junior Faculty to L.M.D. We thank Preethi Gopal, Chloe Noe, Sissi Palma Ribeiro, and Serena Scognamiglio for contributions to early histology experiments and analysis; the Johns Hopkins Bayview Immunomics Core (supported by NIAMS P30 AR-070254), Raffaello Cimbro, and the UCLA Eli and Edythe Broad Center of Regenerative Medicine and Stem Cell Research Flow Cytometry Core for assistance with FACS-based experiments; the UCLA Eli and Edythe Broad Center of Regenerative Medicine and Stem Cell Research Microscopy Core for access to confocal microscopes; and Plexikon for supplying the CSFR1 antagonist PLY5622.

\*E.N.M., D.L., and K.T.H. contributed equally to this work.

The authors declare no competing financial interests.

Correspondence should be addressed to Lindsay M. De Biase at [ldebiase@mednet.ucla.edu](mailto:ldebiase@mednet.ucla.edu).

<https://doi.org/10.1523/JNEUROSCI.1922-21.2022>

Copyright © 2022 the authors

## Introduction

During aging, microglia produce inflammatory factors (DiSabato et al., 2016; Spittau, 2017), induce inflammatory phenotypes in astrocytes (Liddel et al., 2017; Clarke et al., 2018), and exhibit prolonged injury responses (Norden et al., 2015). Cell process motility of microglia also decreases (Damani et al., 2011; Hefendehl et al., 2014), suggesting that microglial-based tissue surveillance and homeostasis are compromised. Finally, signals that promote microglial phagocytosis of synapses increase with aging, and they engulf synapses during presymptomatic neurodegeneration (Stephan et al., 2013; Hong et al., 2016). These findings argue that microglia are likely key determinants of changes in neuronal viability and synaptic function that underlie compromised cognition and movement during aging. Indeed, global manipulation of microglial phenotype during aging can improve cognition (Elmore et al., 2018), and many recently identified risk genes for neurodegenerative disease are

prominently expressed by microglia (Hickman et al., 2018; Sala Frigerio et al., 2019).

Because of their ubiquitous distribution and historically recognized role in immune surveillance, microglia were generally assumed to be equivalent throughout the CNS. We and others recently showed that, instead, microglia in young adult mice display regionally distinct phenotypes (de Haas et al., 2008; Hart et al., 2012; Grabert et al., 2016; De Biase et al., 2017; Ayata et al., 2018; O’Koren et al., 2019), suggesting that tissue homeostasis, microglial injury responses, and microglial modulation of synapses may locally vary. Focusing on basal ganglia circuits, we found that VTA and SNc microglia in young adult mice show lower cell density, simpler morphology, reduced lysosome content, and distinct gene expression compared with striatal and cortical microglia (De Biase et al., 2017). Microglial cell process motility (Stowell et al., 2018), phagocytotic activity (Ayata et al., 2018), and mechanisms of synapse elimination (Gunner et al., 2019) also vary across brain regions in young adult mice.

Do microglia exhibit significant regional heterogeneity in their responses to aging? Given the key role that microglia play in neuroinflammation, responses to CNS insults, and synaptic interactions, prominent regional differences in microglial responses to aging would have critical implications for functional integrity and disease vulnerability of local neuron populations. Pioneering studies have shown that gray and white matter microglia exhibit distinct responses to aging (Safaiyan et al., 2016, 2021) and transcriptome analyses from aging mice reveal key differences in aging-induced changes in microglial gene expression across several brain regions (Grabert et al., 2016). Single-cell RNAseq and FACS-based studies of whole-brain microglia during aging also reveal subsets of microglia with distinct patterns of gene expression and auto-fluorescence during aging (Hammond et al., 2019; Burns et al., 2020), further supporting the idea of heterogeneity in aging responses of these cells. Yet despite these indications that microglial aging is not uniform throughout the CNS, the nature and magnitude of regional differences in microglial aging are largely unexplored, particularly in brain regions with disease-vulnerable populations of neurons.

## Materials and Methods

### Transgenic mice

**C57Bl6 WT mice.** WT mice on the C57Bl6 background were purchased from The Jackson Laboratory (stock #000664).

**CX3CR1<sup>EGFP/+</sup> mice.** CX3CR1<sup>EGFP/EGFP</sup> breeders were originally purchased from The Jackson Laboratory (stock #005582). In these mice, EGFP is knocked in to the CX3CR1 (fractalkine receptor) locus. These mice were maintained on a C57Bl/6 background, and all mice used for experiments were heterozygous (CX3CR1<sup>EGFP/+</sup>), except for analysis of homozygous CX3CR1<sup>EGFP/EGFP</sup> mice. We have shown elsewhere that EGFP expression in the basal ganglia of these mice was specific to microglial cells and 98 ± 1% of Iba1<sup>+</sup> microglia were EGFP<sup>+</sup> (De Biase et al., 2017).

**CX3CR1<sup>CreER-ires-EYFP</sup>; iDTR mice.** Mice expressing inducible cre-recombinase under control of the CX3CR1 promoter (CX3CR1<sup>CreER-ires-EYFP</sup> mice) and mice expressing cre-dependent flox-stop-diphtheria toxin receptor (iDTR mice) were purchased from The Jackson Laboratory (stock #021160 and #007900). Mice used in fate mapping studies were F1 progeny of BALB/cj and CX3CR1<sup>CreER-ires-EYFP</sup>; iDTR mice of C57BL/6J background. Mice were housed, treated with tamoxifen, and killed for tissue collection in the laboratory of Daniel Saban at Duke University.

**ALDH1L1-EGFP mice.** ALDH1L1-EGFP breeders were obtained from Mutant Mouse Resource and Research Centers (MMRRC; stock #011015-UCD) and were originally generated by Gensat. In these BAC transgenic mice, EGFP expression is driven by the astrocyte specific

aldehyde dehydrogenase 1 family member L1 promoter. All mice used for experiments were heterozygous for the transgene.

In all experiments, mice of mixed sex were used, and the number of males and females in each analysis group was balanced. Mice were housed in normal light/dark cycle and had *ad libitum* access to food and water. All experiments were performed in strict accordance with protocols approved by the Animal Care and Use Committees at UCLA, National Institute on Drug Abuse, and Duke.

### Microglial ablation

To pharmacologically ablate microglial cells from the CNS, CX3CR1<sup>EGFP/+</sup> mice age 13–20 months were treated with the CSF1R antagonist PLX5622 (Plexxikon) administered through the diet (1200 mg/kg chow). Mice were maintained on PLX5622 or control AIN-76A diet for 3–4 weeks and were then returned to standard vivarium chow for 3 weeks before tissue collection for immunohistochemistry. Mice that underwent microglial ablation using this approach maintained their body weight during the PLX5622 treatment and subsequent period of microglial repopulation. These mice also appeared normal during qualitative evaluation of motor coordination and exploratory behavior. To confirm microglial cell death and quantify ablation efficacy, tissue was collected from some mice after they had been administered PLX5622 via diet for 7 d.

### Tamoxifen treatments

Tamoxifen (Sigma-Aldrich catalog #T5648) was dissolved in corn oil to a stock concentration of 20 mg/ml. CX3CR1<sup>CreER-ires-EYFP</sup>; iDTR mice were given two intraperitoneal injections of tamoxifen (75 mg/kg) with 1 d in between injections at 2 months of age. Mice were then killed at 2 weeks after the second injection or allowed to age to 20–24 months.

### Tissue collection and immunohistochemistry

Tissue was collected from WT, CX3CR1<sup>EGFP/+</sup>, CX3CR1<sup>EGFP/EGFP</sup>, ALDH1L1-EGFP, or CX3CR1<sup>CreER-ires-EYFP</sup>; iDTR mice between 2 and 24 months of age. Mice were deeply anesthetized with an injection of Euthasol (sodium pentobarbital 150 mg/kg and sodium phenytoin 19.2 mg/kg, Virbac) and perfused transcardially with 1 M PBS followed by ice-cold 4% PFA in 1 M PBS. Microglia show circadian-based changes in morphology (Hayashi et al., 2013); all perfusions for this study were hence performed between 9:00 A.M. and 12:00 P.M. Brain tissue was isolated and postfixed in this solution for 4 h at 4°C and then stored in 1 M PBS with 0.1% sodium azide.

For analysis of neuron number, brains were cryoprotected in 30% sucrose, frozen, and coronal brain sections were prepared on a cryostat at a thickness of 25 μm. Brain sections were collected in series, resulting in three sets of serially collected sections per mouse. One set of serially collected sections per mouse was stained and three sections at standardized anterior-posterior locations were analyzed. For all other analyses, brains were not cryoprotected and coronal brain sections (60 μm thick) were prepared on a vibratome in chilled 1 M PBS. Brain sections were grouped according to well-defined anatomic parameters and for analysis of microglial cell density, microglial fate mapping with DTR, microglial cell morphology, and astrocyte density, three brain sections containing NAc and three brain sections containing VTA were analyzed from each mouse. Brain sections were chosen using well-defined anatomic parameters and were matched for anterior-posterior location.

For immunohistochemistry, free-floating brain sections were permeabilized and blocked in 0.3% Triton X-100 and 5% normal donkey serum in 1 M PBS for 2 h with rotation at room temperature. Sections were incubated with primary antibodies prepared in 0.05% Triton X-100 and 5% normal donkey serum in 1 M PBS at 4°C overnight. Sections were incubated with secondary antibodies prepared in 5% normal donkey serum in 1 M PBS for 2 h at room temperature. Control sections incubated with secondary antibody alone did not result in labeling of cells. Primary antibodies used included the following: chicken anti-GFP (1:1000; Aves, catalog #GFP-1020), goat anti-GFP (1:1000; Frontier Institute, catalog #GFP-Go-Af1480), rabbit anti-Iba1 (1:500; Wako, catalog #019-19741), goat anti-DTR (R&D Systems, AF259), rat anti-CD68 (1:200; clone FA-11, AbD Serotec, catalog #MCA1957), mouse anti-TH (1:5000; Sigma, catalog #T1299), chicken anti-TH (1:500; Aves, catalog #TYH), mouse

anti-NeuN (clone A60, 1:500; Millipore, catalog #MAB377), rat anti-BrdU (1:500; Accurate Chemical and Scientific), and rabbit anti-GFAP (1:500, Agilent Technologies, catalog #Z033429-2). Primary antibodies have been validated for use in immunohistochemistry in mouse tissue in published literature and on the manufacturer's websites. Secondary antibodies used included the following: AlexaFluor-488-, -594-, or -647-conjugated secondary antibodies to rabbit, mouse, goat, chicken, rat, or guinea pig (1:1000; all raised in donkey; Jackson ImmunoResearch Laboratories). A 1:4000 dilution of DAPI in 1 M PBS was used to stain nuclei.

#### Image acquisition and analysis

Fixed tissue was imaged using an Olympus FV1000 confocal microscope, a Zeiss LSM880 confocal microscope, a Zeiss LSM700 confocal microscope, or a Zeiss Apotome microscope. Within the NAc, analyzed images were acquired at the boundary between core and shell (identified anatomically), and include both subregions. In the VTA, analyzed images were medial to the medial lemniscus and included the parabrachial pigmented area, as well as portions of the parafasciculus retroflexus area and paranigral nucleus. For quantification of microglial or astrocyte density, stacks of confocal images (*z* stacks) with a *z* interval of 1.5  $\mu$ m were taken through a 20 $\times$  objective and imported into ImageJ software for analysis. Within ImageJ software, maximum intensity projections of confocal *z* stacks were created and cells were counted manually by creating ROI tags for each cell. X-Y coordinates of all cells in an FOV were extracted from ROI files for use in nearest neighbor analysis. This was accomplished by creating a dissimilarity matrix in OriginPro to calculate distance from each cell to every other cell in the FOV and then determining the minimum distance. For 3D reconstruction of individual microglia, confocal *z* stacks were taken with a 63 $\times$  objective and a *z* interval of 0.3  $\mu$ m and imported into Imaris (Bitplane) software for analysis via filament tracer module; 3 or 4 microglia from separate mice were reconstructed per brain region per age. For quantification of microglial tissue coverage, *z* stacks were taken with a 63 $\times$  objective and a *z* interval of 1.5  $\mu$ m. Within ImageJ software, the mean pixel intensity of the dimmest cell processes was measured at 10–15 locations diagonally across each image. The average of these values was taken as a threshold for determining the % of pixels above (representing microglial cell somas and processes) and below (representing background) this threshold. For 3D reconstruction and analysis of microglial lysosomes, confocal *z* stacks were taken with a 63 $\times$  objective and a *z* interval of 0.3  $\mu$ m. For analysis of microglial lysosomes during normal aging and CX3CR1 KO, microglia and lysosomes were reconstructed in Imaris using surfaces module. For analysis of microglial lysosomes following microglial ablation and repopulation, maximum projection images from confocal *z* stacks were analyzed in ImageJ. Somatic CD68 aggregates were manually traced and measured for area. Lysosome coverage of microglia was calculated using thresholding to measure the number of CD68<sup>+</sup> pixels and EGFP<sup>+</sup> (microglia) pixels for a given FOV. For quantification of neuronal cell loss, tiled *z* stacks of confocal images were taken with a 20 $\times$  objective and a *z* interval of 1.5  $\mu$ m such that the entire VTA and SNc were visualized. Stitched, maximum intensity projections were imported into ImageJ, and cells were counted manually. For all image analyses, three images from separate brain sections were analyzed per mouse to obtain an average value for that mouse. For quantification of neuronal cell loss, the total number of cells across three stereologically matched sections was also calculated. Three to six mice were analyzed per brain region, per age. Sample sizes were selected to be in the upper range of published immunohistochemistry experiments. Experimenters were not blind to source brain region during image analysis.

#### Microdissection

CX3CR1<sup>EGFP/+</sup> mice were anesthetized with Euthasol (sodium pentobarbital 150 mg/kg and sodium phenytoin 19.2 mg/kg, Virbac) and perfused transcardially with 10 ml of oxygenated, ice-cold *N*-methyl-D-glucamine (NMDG)-based solution containing the following (in mM): 92 NMDG, 20 HEPES, 30 NaHCO<sub>3</sub>, 1.2 NaH<sub>2</sub>PO<sub>4</sub>, 2.5 KCl, 5 sodium ascorbate, 3 sodium pyruvate, 2 thiourea, 10 MgSO<sub>4</sub>, and 0.5 CaCl<sub>2</sub>, 10 glucose, pH 7.4 (310 mOsm). Brains were then rapidly dissected free. For qPCR and high-sensitivity ELISA of tissue levels of inflammatory

factors, horizontal midbrain sections (230  $\mu$ m thick) and coronal forebrain sections (300  $\mu$ m thick) were prepared using a vibratome in ice-cold NMDG-based cutting solution bubbled continuously with 95% O<sub>2</sub>/5% CO<sub>2</sub>. After sectioning, slices remained in ice-cold, oxygenated NMDG solution and were transferred one at a time to a glass dissecting surface under a stereoscope maintained at 4°C. The VTA was microdissected from horizontal midbrain sections, and NAc and overlying mPFC were microdissected from coronal forebrain sections using fine-tipped forceps. Microdissected tissue was minced using a scalpel under the stereoscope before being transferred to Eppendorf tubes containing 1 ml NMDG stored on ice. Samples were then centrifuged, NMDG removed, and samples were either flash frozen (for high-sensitivity ELISA protein analysis) or were resuspended in 100  $\mu$ l PicoPure RNA extraction buffer and incubated at 42°C for 30 min and stored in RNase-free tubes at –80°C until further processing (for qPCR analysis). For qPCR of midbrain and striatum tissue following microglial ablation and repopulation, mice were perfused with NMDG. Rough coronal brain sections were then prepared using a brain block, and striatum was microdissected from anterior brain sections while midbrain was dissected from posterior sections. Microdissected samples were minced on a glass surface maintained at 4°C, then transferred to tubes containing chilled 1 $\times$  PBS. Samples were spun down, resuspended in PicoPure RNA extraction buffer, and processed for RNA isolation. For digital droplet PCR (ddPCR) of FACS-isolated microglia, mice were perfused with NMDG, rough coronal brain sections were prepared using a brain block and processed as described below.

#### Tissue dissociation and flow cytometry

The striatum and overlying cortex were microdissected from anterior brain sections, and the midbrain was dissected from posterior sections. Microdissected samples were minced on a glass surface maintained at 4°C. Samples were then transferred to Eppendorf tubes containing 1 ml Hibernate A and were gently dissociated using sequential trituration with fire-polished glass pipettes with openings of decreasing diameter (final pipette ~0.4 mm diameter opening). Resulting cell suspensions were spun down, resuspended in 300  $\mu$ l 1 M PBS, and filtered through a 40  $\mu$ m mesh filter. Throughout the experiment, samples were kept at 4°C on ice. Samples were sorted using a FACS Aria I cell sorter (BD Biosciences). The population of cells containing microglia could be readily identified based on forward scattering (FSC) and side scattering (SSC) properties. A gating strategy based on FSC and SSC width and height was used to select only single cells, and reduce debris, doublets, and dead cells. Microglial cells within this population were then identified and sorted according to EGFP expression as described previously (De Biase et al., 2017). Microglia were FACS sorted directly into Eppendorf tubes containing 50  $\mu$ l PicoPure RNA extraction buffer and, following the sort, samples were incubated at 42°C for 30 min, and stored in RNase-free tubes at –80°C until further processing.

#### RNA extraction and RT-PCR/ddPCR

RNA from microdissected tissues and sorted cells was isolated using the PicoPure RNA isolation kit (Arcturus Bioscience). Column filtration, washing, and elution of RNA from the columns were performed according to the manufacturer's instructions in section C of the PicoPure RNA isolation protocol. RNA concentration and integrity were then analyzed via NanoDrop spectrophotometer. Single-strand cDNAs were synthesized with Superscript III first-strand cDNA synthesis kit (Invitrogen), according to the manufacturer's protocol. For qPCR analysis of tissue levels of gene expression, duplex qPCR assays were performed on technical duplicates using a FAM-labeled probe for each target gene, and a VIC-labeled probe for the endogenous control gene (*Gapdh*), along with TaqMan Advanced Fast PCR Master Mix (catalog #4444963; Invitrogen). To avoid amplification of genomic DNA contamination, primers and probes that amplify across target gene exon–exon junctions were selected when possible. RT-PCRs were run in a 7500 Fast TaqMan instrument or a QuantStudio5 using the program: 95°C hold for 20 s, followed by 40 cycles of 95°C denaturation for 3 s, and 60°C annealing and extension for 30 s. Calculations of relative expression from Ct data were conducted according to User Bulletin #2

for ABI Prism 7900 Sequence Detection System. For each target gene, the average Ct value for the endogenous control (*Gapdh*) was subtracted from the average Ct value for the target gene, to obtain  $\Delta$ Ct. The relative expression was then plotted as  $2^{-\Delta$ Ct}. For ddPCR analysis of tissue levels of inflammatory factors, duplex assays were performed on technical duplicates using a FAM-labeled probe for each target gene, and a VIC-labeled probe for the endogenous control gene (*Gapdh*). Reactions were run in a Bio-Rad QX-200 ddPCR system (Automated Droplet Generator, Thermocycler, and Droplet Reader). Thermocycler conditions were as follows: 95°C hold for 10 min, followed by 40 cycles of 95°C denaturation for 30 s and 60°C annealing and extension for 1 min, with a final 98°C for 30 s and using ddPCR Supermix for Probes (No dUTP). Calculations of absolute expression were made within Quantasoft software according to the manufacturer's recommendations.

#### Protein extraction and MesoScale analysis of cytokines

Serum samples and brain tissue samples were evaluated in duplicate using the V-PLEX Proinflammatory Panel 1 Mouse Kit (catalog #K15048D, Meso Scale Diagnostics), and the following cytokines were assayed in each sample: IFN- $\gamma$ , IL-1 $\beta$ , IL-2, IL-4, IL-5, IL-6, IL-10, IL-12p70, chemokine ligand 1 (CXCL1 or KC/GRO), and TNF $\alpha$ . All samples were assessed following the recommended protocols suggested by the manufacturer. Tissue samples [NAc:  $3.9 \pm 0.9$  mg (mean  $\pm$  SD for all tissues) (2–3 months),  $4.7 \pm 2.2$  mg (17–18 months),  $3.1 \pm 0.5$  mg (22–24 months); VTA:  $2.2 \pm 1.2$  mg (2–3 months),  $2.7 \pm 2$  mg (17–18 months),  $2.1 \pm 0.7$  mg (22–24 months)] were homogenized in small-volume tubes (Tissue homogenizing CKMix\_WP tubes) using a Precellys Evolution plus Cryolys Evolution system (Bertin Instruments). The tissues were homogenized in  $\sim 65$   $\mu$ l of in a Tris-based lysis buffer (MSD Tris Lysis Buffer, catalog #R60TX-3) with protease and phosphatase inhibitors (Halt protease & phosphatase inhibitor single-use cocktail; Thermo Fisher Scientific, catalog #78442). Following homogenization, lysate was extracted from the tube, placed in a fresh Eppendorf tube, and centrifuged ( $10,000 \times g$  for 10 min, 4°C). Thereafter, the supernatant was collected into new tubes. Protein concentrations were then measured by BCA assay (Micro BCA Protein Assay Kit, catalog #23235; Thermo Fisher Scientific). The resulting supernatant yielded low volumes (30–40  $\mu$ l of supernatant) with varying quantities of total protein, for NAc 0.6–5.7  $\mu$ g/ $\mu$ l and for VTA 0.23–1.4  $\mu$ g/ $\mu$ l. Serum samples were diluted 1 in 2 with the kit dilution buffer, and then loaded into the wells of a 96-well multiplex ELISA plate. Cytokine detection signals generated for each sample were compared with a cytokine standard curve, and the serum raw data levels were then calculated by use of Discovery Workbench (Meso Scale Diagnostics) and expressed as pg/ml. Data are shown as a normalized ratio relative to 2- to 3-month-old animals. Tissue samples were mixed with the kit dilution buffer and loaded into the wells of the 96-well multiplex ELISA plate. Because of the low volumes and total protein levels recovered from the samples, samples were loaded into the wells of the ELISAs at different total protein contents. Most NAc samples were loaded at 30  $\mu$ g per well, whereas the loading for NAc samples varied from 15 to 25  $\mu$ g per well, depending on the sample. All VTA samples were loaded at 10  $\mu$ g per well. Cytokine levels in tissues were calculated in the same way as the serum samples.

#### Statistical comparisons

All graphed values are shown as mean  $\pm$  SEM. Statistical details of experiments (statistical tests used, exact value of  $n$ , what  $n$  represents) can be found in Results and the figure legends. In general, statistical significance was assessed using one- or two-way ANOVA. *Post hoc* comparisons were conducted using Student's  $t$  test with Bonferroni correction for multiple comparisons. Data are sufficiently normal and variance within groups is sufficiently similar for use of parametric tests. Paired  $t$  tests were used to compare trends across two different regions within individual mice.

## Results

### VTA microglia show early increases in cell density during aging

Cortical and white matter microglia show significant increases in cell density as mice reach 2 years of age (Hart et al., 2012;

Hefendehl et al., 2014; Safaiyan et al., 2016). Whether increasing microglial abundance during aging is universal or varies across brain regions is largely unexplored. In young adult mice, microglia in distinct basal ganglia nuclei exhibit prominent regional differences in cell attributes, including cell density (De Biase et al., 2017). To determine whether these regional differences in cell density are maintained during aging, we analyzed microglia in the VTA and NAc of aging *CX3CR1*<sup>EGFP/+</sup> mice.

In the NAc, microglial density remained largely consistent at 2, 9, 13, 18, and 22–24 months (Fig. 1A–C). In contrast, in the VTA microglial density showed a slight (nonsignificant) decrease at 9 months of age compared with 2 months and then began to increase at 13 months with further increases evident at 18 and 22–24 months. These increases represent an  $\sim 28\%$  increase in VTA microglial abundance at 18 months and a 42% increase at 22–24 months. Moreover, at 2 and 9 months, microglial density was consistently higher in the NAc than the VTA of the same mouse (Fig. 1D). This inter-region relationship was less significant at 13 months, no longer significant at 18 months, and by 22–24 months, VTA microglial density was similar to and sometimes exceeded that of microglia in the NAc of the same mouse. Similar, region-specific increases in VTA microglial density were observed in C57Bl6 WT mice (Fig. 1E). These findings reveal significant regional variation in expansion of the microglial population during aging. Moreover, they demonstrate that microglial responses to aging begin as early as midlife in select brain regions.

To examine whether increases in VTA microglial density were accompanied by a breakdown in evenly spaced microglial “tiling” of the tissue, we conducted nearest neighbor analysis at 13, 18, and 22–24 months. As expected, average nearest neighbor distance was tightly correlated with average cell density in individual mice (Fig. 1F). Although average nearest neighbor distance tended to decrease with age in the VTA, this did not reach significance ( $p = 0.09$ ) (Fig. 1G). Categorizing cells according to whether their nearest neighbor was extremely close ( $<7.5$   $\mu$ m), relatively close (7.5–20  $\mu$ m), evenly spaced (20–55  $\mu$ m), or abnormally distant ( $>55$   $\mu$ m) revealed that, across all ages analyzed, the majority ( $75 \pm 5\%$ ) of microglia from both regions continued to be evenly spaced across the tissue (Fig. 1H). However, there was a nonsignificant trend toward fewer evenly spaced (20–55  $\mu$ m) microglia at 22–24 months and a significant increase in microglia with extremely close neighbors in both the NAc and VTA at 18 and 22–24 months relative to 13 months, indicating that subtle changes in microglial tissue distribution do occur in both regions starting at 18 months of age.

### Morphologic changes in basal ganglia microglia during aging

Cortical and hippocampal microglia exhibit altered morphology as mice reach 2 years of age and during early stages of neurodegenerative disease (Salter and Stevens, 2017; Wolf et al., 2017; Salas et al., 2020). To define the impact of aging on basal ganglia microglial cell structure, we examined high-magnification images from 2- and 18-month-old *CX3CR1*<sup>EGFP/+</sup> mice. A small percentage of microglia in 18-month-old mice displayed clear morphologic abnormalities in the form of somatic protrusions and cell process inclusions (Fig. 2A). These structures did not contain DAPI<sup>+</sup> nuclei, indicating that they do not represent instances of cell division or engulfment of dying cells. However, these somatic protrusions and cell process inclusions were filled with CD68<sup>+</sup> lysosome material. These structures were observed in  $\sim 3.4 \pm 2\%$  of NAc microglia and  $5.6 \pm 2\%$  of VTA microglia.

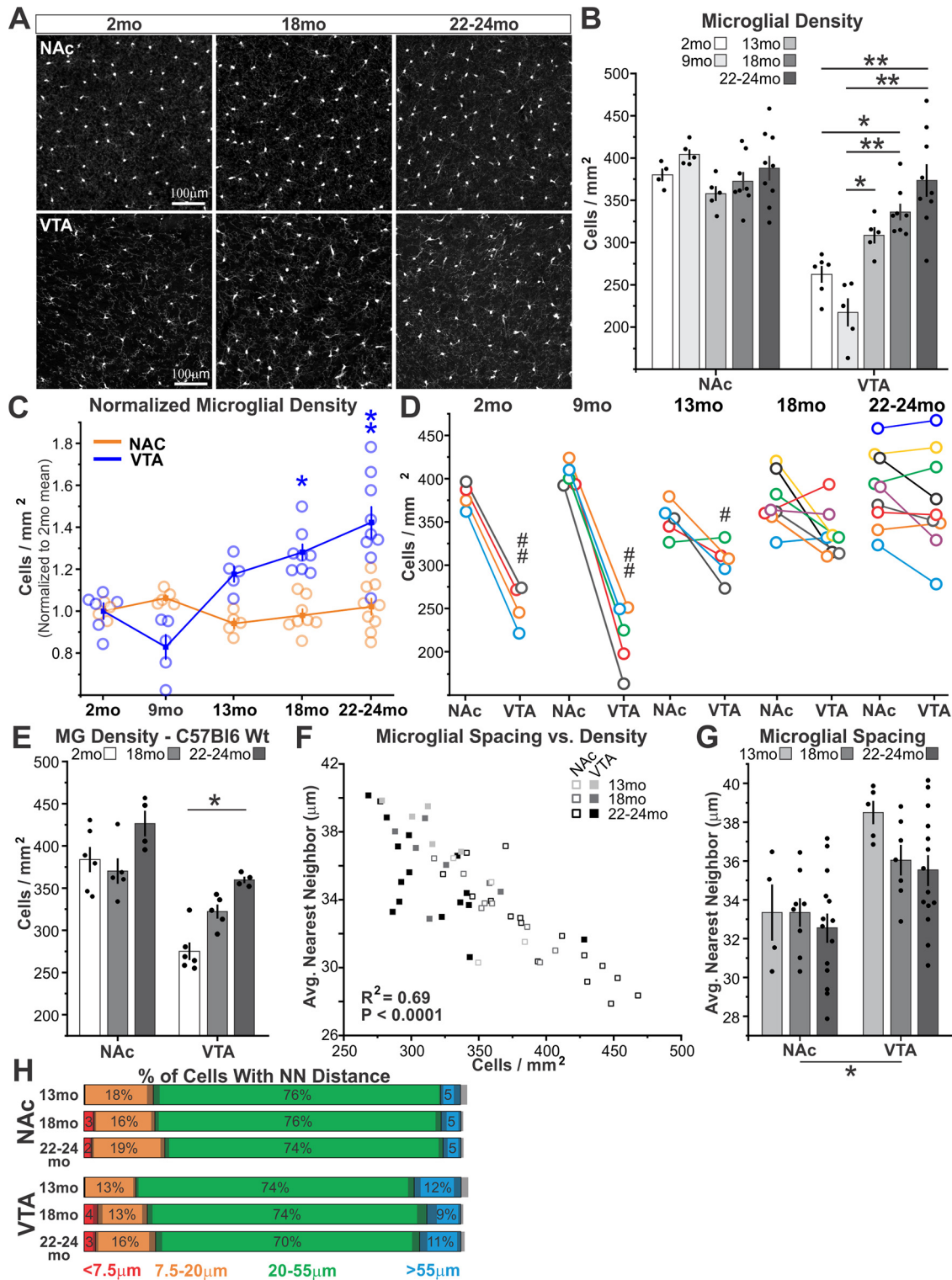


**Figure 1.** VTA microglia show early increases in cell density. **A, B**, Images and quantification of NAc and VTA microglial density in 2-, 9-, 13-, 18-, and 22- to 24-month (mo)-old *CX3CR1<sup>EGFP/+</sup>* mice. Two-way ANOVA: main effect of age,  $F_{(4,63)} = 8.5, p < 0.0001$ ; main effect of brain region,  $F_{(1,63)} = 77.5, p < 0.0001$ ; interaction,  $F_{(4,63)} = 11.8, p < 0.0001$ . **C**, NAc and VTA microglial density during aging normalized to values observed in 2-month-old animals. Two-way ANOVA: main effect of age,  $F_{(3,53)} = 10.8, p < 0.0001$ ; main effect of brain region,  $F_{(1,53)} = 24.1, p < 0.0001$ ; interaction,  $F_{(3,53)} = 14.3, p < 0.0001$ . **D**, Comparison of NAc and VTA microglial density within individual mice at different ages. Data points from the same mouse colored alike. ##  $p < 0.0001$ ; #  $p < 0.05$ ; two-tailed paired *t* test. **E**, Microglial (MG) density during aging in C57Bl6 WT mice. Two-way ANOVA: main effect of age,  $F_{(2,29)} = 12.7, p = 0.0002$ ; main effect of brain region,  $F_{(1,29)} = 51.5, p < 0.0001$ ; interaction,  $F_{(2,29)} = 3.4, p = 0.05, n.s.$  **F**, Linear regression analysis of the relationship between microglial cell density and average microglial nearest neighbor distance. **G**, Average (Avg.) nearest neighbor distance for NAc and VTA microglia during aging. Two-way ANOVA: main effect of age,  $F_{(2,51)} = 1.9, p = 0.17, n.s.$ ; main effect of brain region,  $F_{(1,51)} = 20.2, p < 0.0001$ ; interaction,  $F_{(2,51)} = 0.7, p = 0.49, n.s.$  **H**, Percentage of microglia that fall into different nearest neighbor (NN) distance categories. Gray shading represents SEM. Two-way ANOVA for  $< 7.5 \mu\text{m}$ : main effect of age,  $F_{(2,51)} = 5.3, p = 0.008$ ; main effect of brain region,  $F_{(1,51)} = 0.81, p = 0.37, n.s.$ ; interaction,  $F_{(2,51)} = 0.17, p = 0.84, n.s.$  \* $p < 0.05$ , \*\* $p < 0.0001$ .

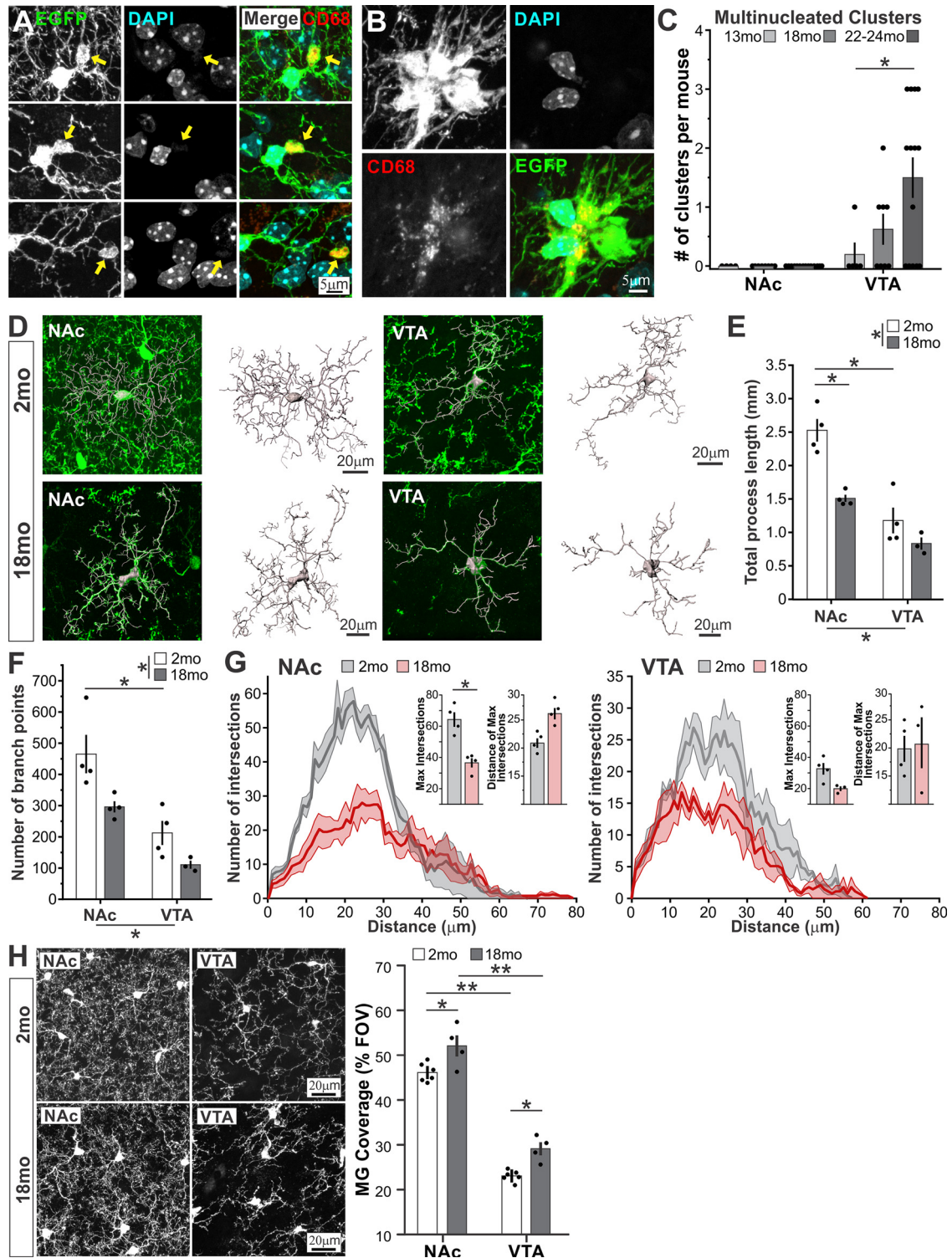


**Figure 2.** Morphologic rearrangements in microglia emerge by late middle age. **A**, Examples of somatic swellings and cell process inclusions (yellow arrows) from NAc and VTA microglia of 18-month (mo)-old  $CX3CR1^{EGFP/+}$  mice. **B**, Example of microglial clusters observed in VTA of 18-month-old  $CX3CR1^{EGFP/+}$  mice. Costaining with DAPI and CD68 reveals that clusters do not contain engulfed pyknotic nuclei and CD68 staining is abundant within the cluster. **C**, Frequency of multinucleated microglial clusters observed in NAc and VTA during aging. Two-way ANOVA: main effect of age,  $F_{(2,52)} = 3.3$ ,  $p = 0.04$ ; main effect of brain region,  $F_{(1,52)} = 11.5$ ,  $p = 0.001$ ; interaction,  $F_{(2,52)} = 3.3$ ,  $p = 0.04$ . **D**, Reconstruction of individual NAc and VTA microglia in 2- and 18-month-old  $CX3CR1^{EGFP/+}$  mice. **E**, Total cell process length of reconstructed microglia. Two-way ANOVA: main effect of age,  $F_{(1,14)} = 21.5$ ,  $p = 0.0007$ ; main effect of brain region,  $F_{(1,14)} = 47.5$ ,  $p < 0.0001$ ; interaction,  $F_{(1,14)} = 5.3$ ,  $p = 0.04$ . **F**, Number of branch points for reconstructed microglia. Two-way ANOVA: main effect of age,  $F_{(1,14)} = 10.9$ ,  $p = 0.007$ ; main effect of brain region,  $F_{(1,14)} = 28.5$ ,  $p = 0.0002$ ; interaction,  $F_{(1,14)} = 0.67$ ,  $p = 0.43$ , n.s. **G**, Sholl analysis of reconstructed NAc and VTA microglia. Insets, Maximum number of intersections and the distance at which maximum intersections occur in each region. **H**, Percent coverage of the field of view (FOV) by microglial somas and processes. Two-way ANOVA: main effect of age,  $F_{(1,19)} = 23.4$ ,  $p = 0.0002$ ; main effect of brain region,  $F_{(1,19)} = 338.6$ ,  $p < 0.0001$ ; interaction,  $F_{(1,19)} = 0.004$ ,  $p = 0.95$ , n.s. \* $p < 0.05$ . \*\* $p < 0.0001$ .

An additional microglial morphologic abnormality observed in the VTA of aging mice were apparent “clusters” of microglial cells (Fig. 2B). Analysis of 13, 18, and 22 to 24 month-old mice indicated that the frequency of these microglial clusters increases progressively with age in the VTA, while microglial clusters were not observed in the NAc (Fig. 2C). Although these clusters appeared to contain many microglial cells, colabeling with DAPI revealed that they typically only contained a small number of microglia that had elaborated an extensive membrane surface. No pyknotic nuclei indicative of dying cells were observed within these structures, and they were not filled with TH<sup>+</sup> material as one might expect if large portions of dopamine neurons had been phagocytosed. However, they did contain abundant CD68<sup>+</sup> lysosomes, suggesting degradation of some form of engulfed material.

Aside from these overt morphologic abnormalities, the majority of microglia in both the NAc and VTA were still highly ramified and did not show obvious signs of morphologic “activation” at 18 months. To determine whether subtle changes in cell structure were present in these cells, we reconstructed the morphology of individual microglia that did not exhibit overt morphologic abnormalities using Imaris (Fig. 2D). Consistent with our published studies (De Biase et al., 2017), microglia in the NAc of young adult mice had significantly greater total process length and process branch points than VTA microglia (Fig. 2E, F). In both NAc and VTA, total process length and process branching was reduced at 18 months, suggesting that both regions are likely to experience changes in microglial tissue surveillance and dynamic interactions of microglia with surrounding structures. Sholl analysis confirmed reductions in microglial cell branching complexity with age, while indicating that overall cell territory size remained relatively constant (Fig. 2G). Despite these decreases in total process length and process branching of individual cells, microglial tissue coverage (the extent to which microglial processes and somas covered the FOV) increased slightly in both regions at 18 months (Fig. 2H). Increased tissue coverage is likely because of increased cell process thickness and, in the VTA, an increased number of cells occupying the brain region. Collectively, these findings indicate that changes in microglial morphology are detectable by late middle age in both the NAc and VTA, but that instances of morphologic abnormality, such as multinucleated microglial cell clusters, are more common in the VTA and decreases in branching complexity are slightly more prominent in the NAc.

### Inflammatory profile of midbrain microglia emerges by 13 months of age

Our analyses of microglial density indicate that the VTA microglial population begins to change between 9 and 13 months of age. To determine whether important shifts in the functional state of VTA microglia also occur during this time period, we microdissected midbrain (containing VTA), striatum (containing NAc), and cortex from acute brain sections. We then FACS-isolated microglia, and analyzed expression of key inflammatory factors via ddPCR (Fig. 3A). Analysis of FSC during FACS did not reveal any significant changes in cell soma size between 2 and 13 months of age in any region analyzed (Fig. 3B). However, analysis of SSC showed significant increases in all regions analyzed at 13 months (Fig. 3C), indicating that, by midlife, elevated internal complexity or granularity is evident in microglia across multiple CNS regions. Intriguingly, these increases in SSC were more pronounced in midbrain microglia than cortex or striatum microglia (Fig. 3C,D).

Analysis via ddPCR revealed that microglial expression of TNF $\alpha$  tended to be greater in the midbrain compared with the striatum and cortex (Fig. 3E). Within individual mice, no significant differences across region were observed in 2-month-old mice (Fig. 3E). In contrast, in 13-month-old mice, midbrain microglia expressed significantly higher levels of TNF $\alpha$  transcript than striatal or cortical microglia from the same mouse. No significant differences in levels of IL-1 $\beta$  were observed across brain region or age (Fig. 3F). These analyses suggest that early expansion of the VTA microglial population is accompanied by increases in intracellular granularity and increased expression of select inflammatory factors, raising the possibility that regional differences in local CNS inflammation could arise as early as midlife.

### Local increases in inflammation parallel expansion of the VTA microglial population

To further explore the relationship between microglial population expansion and local, aging-induced CNS inflammation, we microdissected NAc and VTA tissue from 2-, 18-, and 22- to 24-month-old CX3CR1<sup>EGFP/+</sup> mice, and used qPCR to examine levels of TNF $\alpha$  and IL-1 $\beta$  at the tissue level (Fig. 4A–C). We also analyzed microdissected mPFC, which is known to show increased inflammation during aging (Lu et al., 2004; Primiani et al., 2014). At 24 months of age, TNF $\alpha$  and IL-1 $\beta$  showed a trend toward increased levels of expression within mPFC, and in the NAc and VTA, these increases were significant. Moreover, increases in TNF $\alpha$  and IL-1 $\beta$  were already significant at 18 months of age within the VTA (Fig. 4B). These regional differences in expression of inflammatory factors were particularly evident when comparing expression across regions within individual mice (Fig. 4C). At 2 months of age, levels of TNF $\alpha$  and IL-1 $\beta$  were consistently greater in the mPFC than in the NAc or VTA. Instead, at 22–24 months of age, levels of TNF $\alpha$  and IL-1 $\beta$  in the VTA were consistently greater than those observed in the NAc and mPFC of the same mouse.

To examine local inflammation at the protein level, we microdissected NAc and VTA tissue from 2, 18, and 22 to 24 month-old CX3CR1<sup>EGFP/+</sup> mice and used high-sensitivity ELISA arrays to examine a panel of pro- and anti-inflammatory cytokines. Multiple pro- and anti-inflammatory cytokines were found at higher concentrations in the VTA compared with the NAc at all ages examined (Fig. 4D). These included TNF $\alpha$ , IL-1 $\beta$ , IL-5, IL-6, IFN $\gamma$ , and IL-10. In the VTA, TNF $\alpha$  was further modulated by age, showing significant increases in tissue concentration at 22–24 months relative to 2 months. Some factors, such as chemokine ligand 1 (CXCL1; KC/GRO), were found at similar levels across both regions and were not modulated by age. Collectively, these analyses suggest that inflammatory signaling is elevated locally within VTA and that this local elevation is further exacerbated during aging.

### Similar aging-induced changes are evident in SNc microglia

Midbrain dopamine neurons are particularly vulnerable to functional decline and neurodegenerative disease during aging (Brichta and Greengard, 2014; Fu et al., 2018). The underlying causes of this vulnerability are still poorly understood. Although dopamine neurons in the VTA exhibit elevated disease susceptibility, dopamine neurons in the SNc are typically even more vulnerable to damage and decline (Brichta and Greengard, 2014). To explore whether similar, aging-induced changes in microglial phenotype are observed in the SNc, we examined microglial density and morphology within the SNc of CX3CR1<sup>EGFP/+</sup> mice.



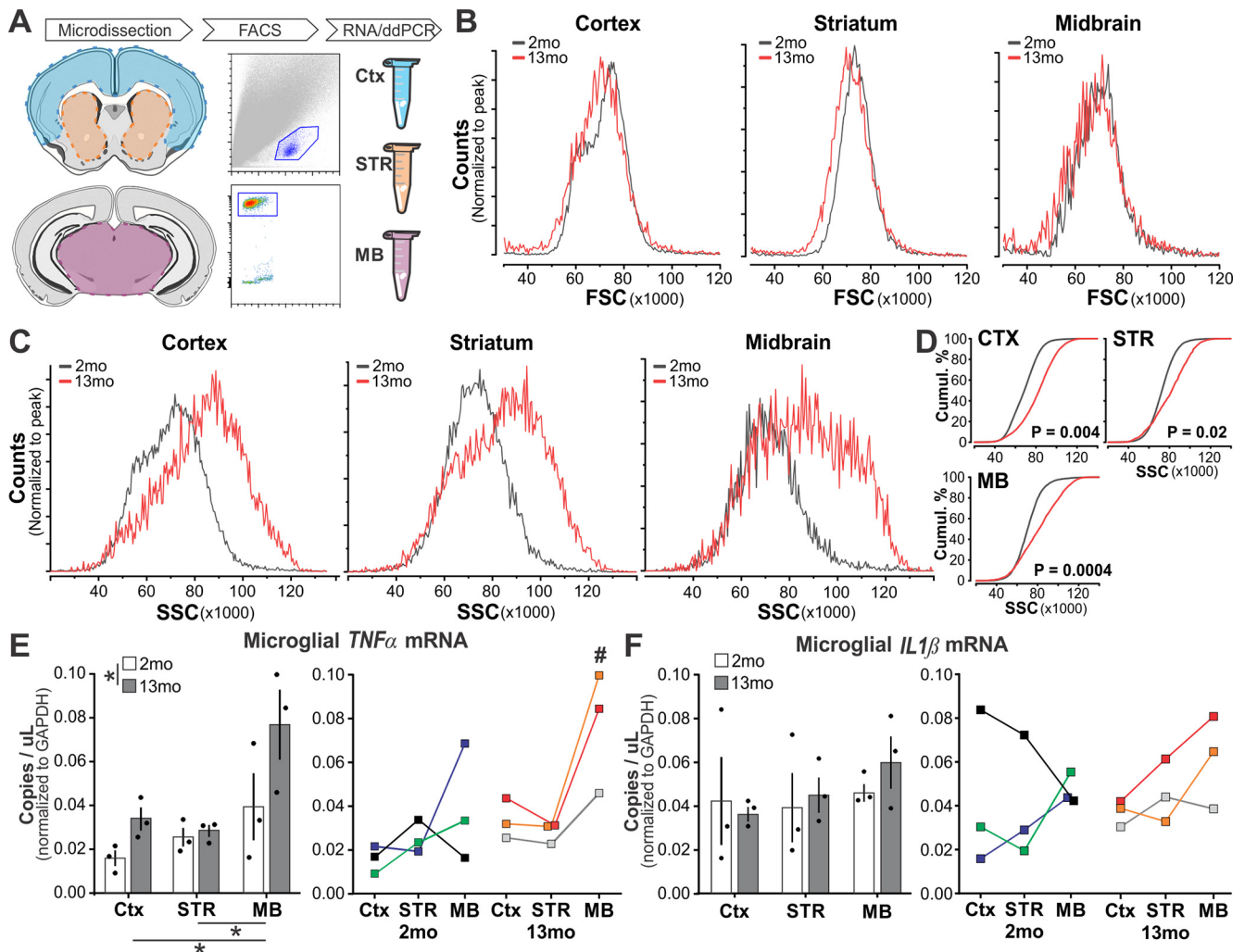


**Figure 3.** Local increases in VTA microglial inflammation begin as early as middle age. **A**, Workflow schematic; midbrain (MB), striatum (STR), and cortex (CTX) were dissected from acute coronal forebrain sections followed by FACS isolation of EGFP<sup>+</sup> microglia, RNA extraction, and ddPCR analysis. **B**, **C**, Histograms comparing FSC and SSC of microglia from 2- and 13-month-old mice in each brain region. **D**, Cumulative probability distributions comparing SSC of microglia in 2- and 13-month-old mice from each brain region. **E**, Left, Microglial expression of *TNF $\alpha$*  transcript. Two-way ANOVA: main effect of age,  $F_{(1,17)} = 6.1$ ,  $p = 0.03$ ; main effect of brain region,  $F_{(2,17)} = 7.5$ ,  $p = 0.008$ ; interaction,  $F_{(2,17)} = 1.6$ ,  $p = 0.24$ , n.s. Right, Comparison of NAc and VTA microglial *TNF $\alpha$*  expression within individual mice at 2 and 13 months. Data points from same mouse are colored alike. # $p < 0.05$  (paired *t* test). **F**, Left, Microglial expression of *IL-1 $\beta$*  transcript. Two-way ANOVA: main effect of age,  $F_{(1,17)} = 0.2$ ,  $p = 0.66$ ; main effect of brain region,  $F_{(2,17)} = 0.7$ ,  $p = 0.51$ ; interaction,  $F_{(2,17)} = 0.34$ ,  $p = 0.72$ , n.s. Right, Comparison of NAc and VTA microglial *IL-1 $\beta$*  expression within individual mice at 2 and 13 months. Data points from same mouse are colored alike. \* $p < 0.05$ .

Microglial density in the SNc was also significantly elevated at 18 months and remained elevated at 22–24 months (Fig. 5A,B). When normalized to densities in 2-month-old mice, the increases in microglial density in the SNc were of similar magnitude to those in the VTA (Fig. 5C).

Similar to observations in NAc and VTA, analysis of high-magnification images revealed that morphologic abnormalities were also evident in a small percentage of SNc microglia (Fig. 5D). Frequency of microglia with somatic protrusions and cell process inclusions was  $5.7 \pm 2\%$  and  $8.0 \pm 3\%$ , respectively, similar to frequencies observed in VTA ( $5.6 \pm 2\%$  and  $6.1 \pm 4\%$ , respectively). There was also an  $\sim 1.2$ -fold increase in microglial tissue coverage by 18 months in the SNc (Fig. 5E). Finally, multinucleated microglial “clusters” were also observed in the SNc of most mice at 18 months of age and were occasionally quite large (Fig. 5F). Similar to observations in the VTA, these clusters did not contain pyknotic nuclei indicative of dying cells but did contain abundant CD68<sup>+</sup> lysosomes (Fig. 5G). Collectively, these analyses indicate that changes

in the SNc microglial population during aging closely parallel those observed in VTA microglia.

### Resident microglia proliferate to drive expansion of the microglial population during aging

We next sought to identify the mechanisms driving early expansion of the VTA microglial population. To determine whether expansion of the VTA microglial population was driven by proliferation of CNS resident microglia or infiltration of peripheral monocytes that adopt microglial-like attributes, we first treated 18-month-old *CX3CR1<sup>EGFP/+</sup>* mice with BrdU. In both the NAc and VTA, morphologic profiles of dividing cells as well as EGFP<sup>+</sup>BrdU<sup>+</sup> microglia could be observed (Fig. 6A,B), suggesting that proliferation of resident microglia contributes to increases in microglial density during aging. Next, we used genetic approaches to tag microglia during young adulthood and to track their fate during aging. *CX3CR1<sup>CreER-ires-EYFP</sup>* mice were crossed to mice expressing diphtheria toxin receptor (DTR) preceded by a floxed-stopper module (*iDTR* mice). Double-transgenic *CX3CR1<sup>CreER-ires-EYFP</sup>;iDTR* mice were injected with

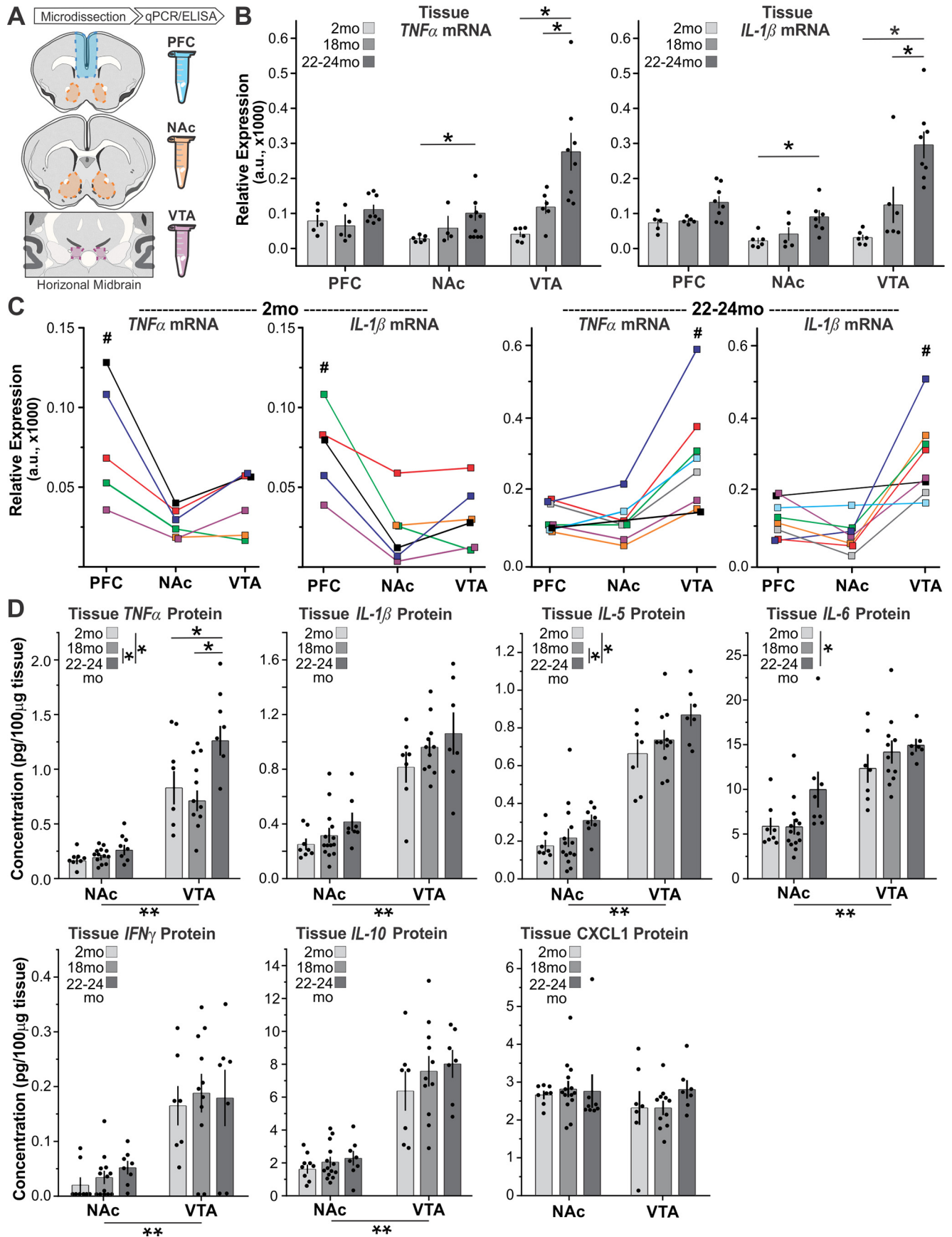


**Figure 4.** Local increases in microglial density are associated with local elevations in inflammation. **A**, Diagram represents regions microdissected for mRNA and protein-level analysis in the PFC, NAc, and VTA. **B**, Relative expression of *TNF $\alpha$*  (left) and *IL-1 $\beta$*  (right) mRNA in the PFC, NAc, and VTA at 2, 18, and 22–24 months (mo). Two-way ANOVAS: *TNF $\alpha$*  main effect of age,  $F_{(2,54)} = 14.1$ ,  $p < 0.0001$ ; main effect of brain region,  $F_{(2,54)} = 6.9$ ,  $p = 0.002$ ; interaction,  $F_{(4,54)} = 4.0$ ,  $p = 0.007$ ; *IL-1 $\beta$*  main effect of age,  $F_{(2,56)} = 8.4$ ,  $p = 0.0007$ ; main effect of brain

tamoxifen at 2 months of age and killed 2 weeks later or allowed to age to 20–24 months. Because mice do not normally express DTR, expression of this receptor acts as a “tag” to label microglia (O’Koren et al., 2019) that were present in the CNS at 2 months of age (Fig. 6C).

In mice killed 2 weeks after tamoxifen injection, 95% of Iba1<sup>+</sup> or EYFP<sup>+</sup> microglia were DTR<sup>+</sup>, demonstrating high recombination efficiency that allows tracking of the majority of microglia and any resulting progeny during aging (Fig. 6D). In mice that were killed at 20–24 months of age, overall microglial density had increased, consistent with observations in CX3CR1<sup>EGFP/+</sup> mice (Fig. 6E). In 20 to 24 month-old mice, 95% of Iba1<sup>+</sup> or EYFP<sup>+</sup> microglia were also DTR<sup>+</sup> (Fig. 6D). Maintenance of this percentage of DTR<sup>+</sup> microglia in aged tissue would only be possible if microglia tagged at 2 months of age played a dominant role in proliferating and expanding the cell population. Indeed, the density of DTR<sup>+</sup> microglia increased during aging (Fig. 6F) and the fold change increase in DTR<sup>+</sup> microglia was almost identical to the fold change increase in density of the total microglial population (Fig. 6G). Furthermore, DTR<sup>+</sup> cells exhibiting morphologic profiles of cell division were evident in aged mice (Fig. 6H). While these analyses do not rule out the possibility that peripheral cells can enter the CNS during aging and adopt microglial phenotypes (Ginhoux et al., 2013; Baufeld et al., 2018), they indicate that the majority of observed microglial population expansion is driven by proliferation of CNS resident microglia.

It is worth noting that we observed a significant increase in NAc microglial density in these mice by 20–24 months of age, which we did not observe in the CX3CR1<sup>EGFP/+</sup> mice. The CX3CR1<sup>CreER-ires-EYFP</sup>; *iDTR* mice and the CX3CR1<sup>EGFP/+</sup> mice used in this study were aged in different vivariums and are on slightly different background strains (50% C57Bl6 50% BALB/cJ for CX3CR1<sup>CreER-ires-EYFP</sup>; *iDTR* mice and 100% C57Bl6 for the CX3CR1<sup>EGFP/+</sup> mice). These observations raise the possibility that environment and genetic background may shape the overall timing and extent of microglial proliferation during aging.

### Aging-induced changes in VTA/SNc microglia precede systemic inflammation, local changes in astrocyte abundance, and parallel early loss of neurons

Systemic inflammation increases with aging and regional differences in CNS penetration of peripheral cytokines (Kennedy and Silver, 2015) could potentially contribute to early changes in VTA/SNc microglial phenotype. To explore this possibility, we measured serum levels of inflammatory signaling factors using

high-sensitivity ELISA cytokine arrays in 2, 18, and 22 to 24 month-old CX3CR1<sup>EGFP/+</sup> mice. Multiple pro-inflammatory factors, such as TNF $\alpha$ , IL-6, and IFN $\gamma$ , were significantly increased during aging (Fig. 7A–J). Several factors that have a mix of pro- and anti-inflammatory functions or largely anti-inflammatory functions were also elevated during aging, including IL-10, CXCL1 (KC/GRO), and IL-2. Other factors, such as IL-1 $\beta$ , IL-4, and IL-5, were detected but did not show significant changes across the ages sampled. In all cases where serum cytokines increased during aging, *post hoc* analyses revealed that these increases did not reach significance until 24 months. These data suggest that regional differences in CNS penetration of peripheral cytokines are unlikely to underlie early changes in VTA/SNc microglial phenotype and population expansion observed at 13–18 months of age.

CNS astrocytes make critical contributions to tissue homeostasis, produce inflammatory factors, and proliferate in response to CNS perturbations (Salas et al., 2020). Microglia and astrocytes can regulate one another’s attributes (Vainchtein and Molofsky, 2020), and local abundance of basal ganglia microglia is tightly correlated with astrocyte density in young adult mice (De Biase et al., 2017). To explore whether regional differences in astrocyte responses to aging could promote regional differences in microglial aging, we examined astrocytes in young adult and aging ALDH1L1-EGFP mice (Fig. 8A). Astrocyte cell density remained relatively stable in the NAc and VTA between 2 and 24 months of age (Fig. 8B), with a trend toward decreased astrocyte abundance in the NAc at 24 months. To examine the functional state of aging NAc and VTA astrocytes, we dissected striatum (containing NAc) and midbrain (containing VTA) from acute brain sections of 2-month-old and 16 to 20 month-old mice, an age range when VTA microglia begin exhibiting clear responses to aging. We then conducted qPCR analysis of *Gfap*, a marker of astrocyte reactivity, and *Glt1* (*Slc1a2*), a key glutamate transporter by which homeostatic astrocytes support synaptic function (Fig. 8C–E). This analysis revealed trends toward increased *Gfap* transcript in striatum and midbrain during aging, but these did not reach significance. No differences were observed in levels of *Glt1* transcript across region or age. Immunostaining-based analysis of GFAP expression at the protein level yielded similar results (Fig. 8F,G); extent of GFAP tissue coverage did not differ significantly across the NAc and VTA and increases in GFAP only reached significance at 22–24 months when pooling across regions. Qualitatively, there did not appear to be a spatial relationship between the distribution of microglia relative to GFAP-expressing astrocytes in the aging VTA and NAc (Fig. 8H). Quantification revealed that the percentage of GFAP<sup>+</sup> astrocytes with nearby microglia (<20  $\mu$ m) increased slightly with age but did not differ across regions and did not exceed 50%, suggesting that instances of close proximity between GFAP<sup>+</sup> astrocytes and microglia are due only to chance (Fig. 8I). While these observations do not rule out that important changes in astrocyte functional state can occur in these brain regions during aging, they argue that regional differences in astrocyte responses to aging are unlikely to be driving early aging phenotypes of VTA microglia that emerge at 13 months of age.

Microglia respond to the death of nearby neurons with numerous changes in cell attributes. Because dopamine neurons are more susceptible to functional decline, early loss of these vulnerable neurons could potentially underlie early responses of VTA/SNc microglia to aging. To explore this possibility, we used two approaches to quantify the abundance of dopamine neurons in the VTA and SNc at 2, 18, and 22–24 months in CX3CR1<sup>EGFP/+</sup>

←

region,  $F_{(2,56)} = 5.2$ ,  $p = 0.009$ ; interaction,  $F_{(4,56)} = 3.3$ ,  $p = 0.02$ . **C**, Comparison of TNF $\alpha$  and IL-1 $\beta$  transcript across brain regions in individual mice. For each age, data points from the same mouse are colored alike. <sup>#</sup> $p < 0.02$ , compared with both other brain regions (paired *t* test). **D**, Local protein levels as measured by high-sensitivity ELISA. Two-way ANOVAS: TNF $\alpha$  main effect of age,  $F_{(2,53)} = 8.8$ ,  $p = 0.0005$ ; main effect of brain region,  $F_{(1,53)} = 126.9$ ,  $p < 0.0001$ ; interaction,  $F_{(2,53)} = 5.0$ ,  $p = 0.01$ ; IL-1 $\beta$  main effect of age,  $F_{(2,54)} = 3.0$ ,  $p = 0.06$ , n.s.; main effect of brain region,  $F_{(1,54)} = 95.1$ ,  $p < 0.0001$ ; interaction,  $F_{(2,54)} = 0.2$ ,  $p = 0.8$ , n.s.; IL-5 main effect of age,  $F_{(2,54)} = 5.2$ ,  $p = 0.009$ ; main effect of brain region,  $F_{(1,54)} = 161.0$ ,  $p < 0.0001$ ; interaction,  $F_{(2,54)} = 0.21$ ,  $p = 0.81$ , n.s.; IL-6 main effect of age,  $F_{(2,54)} = 3.6$ ,  $p = 0.03$ ; main effect of brain region,  $F_{(1,54)} = 44.2$ ,  $p < 0.0001$ ; interaction,  $F_{(2,54)} = 1.1$ ,  $p = 0.34$ , n.s.; IFN $\gamma$  main effect of age,  $F_{(2,53)} = 0.35$ ,  $p = 0.7$ , n.s.; main effect of brain region,  $F_{(1,53)} = 38.7$ ,  $p < 0.0001$ ; interaction,  $F_{(2,53)} = 0.12$ ,  $p = 0.88$ , n.s.; IL-10 main effect of age,  $F_{(2,54)} = 1.3$ ,  $p = 0.27$ , n.s.; main effect of brain region,  $F_{(1,54)} = 91.0$ ,  $p < 0.0001$ ; interaction,  $F_{(2,54)} = 0.25$ ,  $p = 0.78$ , n.s.; CXCL1: main effect of age,  $F_{(2,54)} = 0.6$ ,  $p = 0.56$ , n.s.; main effect of brain region,  $F_{(1,54)} = 1.5$ ,  $p = 0.23$ , n.s.; interaction,  $F_{(2,54)} = 0.6$ ,  $p = 0.057$ , n.s. \* $p < 0.05$ . \*\* $p < 0.0001$ .

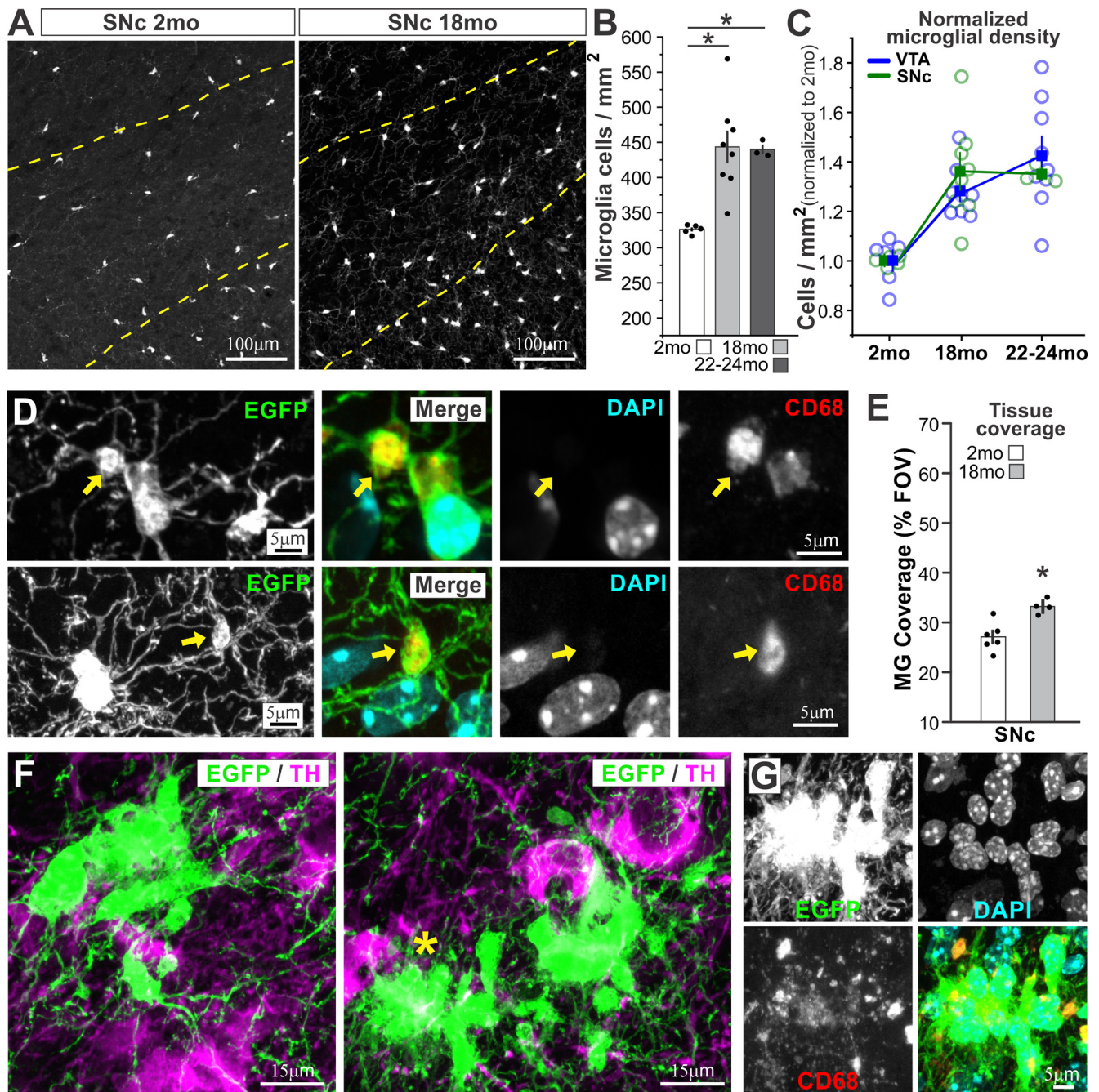


**Figure 5.** SNc microglia resemble VTA microglia during aging and also exhibit multinucleated microglial clusters. **A**, Representative images of microglia in the SNc of 2- and 18-month-old  $CX3CR1^{EGFP/+}$  mice that were used for quantification of microglial density. Dashed yellow line indicates the boundary of the SNc. **B**, SNc microglial density in 2, 18, and 22 to 24 month-old  $CX3CR1^{EGFP/+}$  mice. One-way ANOVA:  $F_{(2,15)} = 9.9$ ,  $p = 0.002$ . **C**, Comparison of VTA and SNc microglial density increases during aging. Densities are normalized to values in each region at 2 months of age. Two-way ANOVA: main effect of age,  $F_{(2,38)} = 19.1$ ,  $p < 0.0001$ ; main effect of brain region,  $F_{(1,38)} = 0.001$ ,  $p = 0.97$ , n.s.; interaction,  $F_{(2,38)} = 0.7$ ,  $p = 0.49$ . **D**, Examples of somatic protrusions (top panels) and cell process inclusions (bottom panels) from SNc microglia in 18-month-old  $CX3CR1^{EGFP/+}$  mice. Yellow arrows and containing with DAPI and CD68 indicate that these structures contain lysosomes but not pyknotic nuclei. **E**, Percent coverage of field of view (FOV) by microglial somas and processes. \* $p = 0.005$  (two-sample  $t$  test). **F**, Examples of multinucleated microglial clusters observed in SNc of 18-month-old  $CX3CR1^{EGFP/+}$  mice. **G**, Costaining of cluster marked with yellow asterisk in **F** with DAPI and CD68, revealing that the clusters do not appear to contain engulfed pyknotic nuclei and that CD68 staining is abundant within the cluster.

mice (Fig. 9A). Quantification of the total number of dopamine neurons ( $NeuN^{+}TH^{+}$ ) in stereologically matched brain sections (Fig. 9B) revealed trends toward reduced numbers of dopamine neurons at 18 and 22–24 months, but these were not significant (Fig. 9C). Quantification of cell density revealed decreases in dopamine neuron cell density that were significant only when pooling data across the VTA and SNc (Fig. 9D), suggesting that loss of dopamine neurons is relatively minor at the ages examined. The

VTA and the SNc also contain non-dopamine, glutamatergic and GABAergic neurons (Brichta and Greengard, 2014; Morales and Margolis, 2017). Although we cannot distinguish glutamatergic from GABAergic neurons, we sought to detect any major cell death within these neuron populations by quantifying the abundance of  $NeuN^{+}TH^{-}$  cells. These non-dopaminergic neurons also showed trends toward reduced total cell number in stereologically matched brain sections and slight but significant reductions in cell density

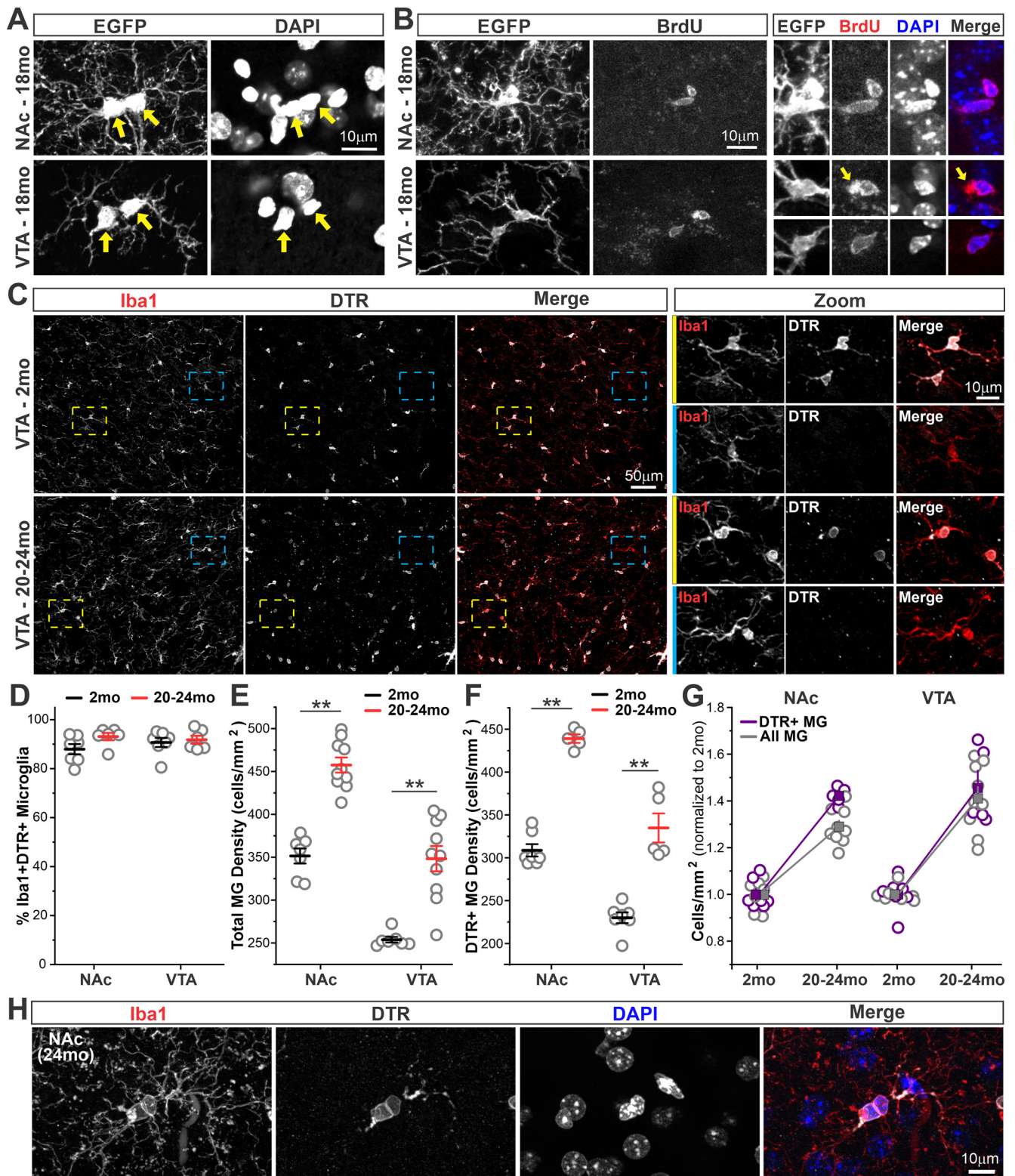


**Figure 6.** Increases in microglial density during aging arise from proliferation of resident microglia. **A**, Microglia exhibiting morphologic profiles of cell division during aging. Yellow arrows indicate closely approximated or interconnected microglial somas with distinct DAPI<sup>+</sup> nuclei. **B**, Examples of BrdU<sup>+</sup> microglia during aging. Yellow arrows indicate lipofuscin autofluorescence that is easily distinguished from BrdU labeling of cell nuclei. **C**, Images from VTA of 2 and 20 to 24 month (mo) old *CX3CR1<sup>CreER-IRES-EYFP</sup>;iDTR* mice treated with tamoxifen at 2 months of age to label microglia present in the CNS at young adult ages. Examples of Iba1<sup>+</sup>DTR<sup>+</sup> microglia (yellow boxes) and Iba1<sup>+</sup>DTR<sup>-</sup> microglia (cyan boxes) shown at higher magnification at right. **D**, % of Iba1<sup>+</sup> microglia that are also DTR<sup>+</sup>. Two-way ANOVA: main effect of age,  $F_{(1,25)} = 2.9$ ,  $p = 0.1$ , n.s.; main effect of brain region,  $F_{(1,25)} = 0.16$ ,  $p = 0.69$ , n.s.; interaction,  $F_{(1,25)} = 1.2$ ,  $p = 0.28$ , n.s. **E**, Quantification of density of all microglia during aging in *CX3CR1<sup>CreER-IRES-EYFP</sup>;iDTR* mice. Two-way ANOVA: main effect of age,  $F_{(1,32)} = 78.8$ ,  $p < 0.0001$ ; main effect of brain region,  $F_{(1,32)} = 81.6$ ,  $p < 0.0001$ ; interaction,  $F_{(1,32)} = 0.2$ ,  $p = 0.67$ , n.s. **F**, Quantification of the density of DTR<sup>+</sup> “tagged” microglia during aging in *CX3CR1<sup>CreER-IRES-EYFP</sup>;iDTR* mice. Two-way ANOVA: main effect of age,  $F_{(1,23)} = 160.3$ ,  $p < 0.0001$ ; main effect of brain region,  $F_{(1,23)} = 96.9$ ,  $p < 0.0001$ ; interaction,  $F_{(1,23)} = 1.9$ ,  $p = 0.18$ , n.s. **G**, Density increases in Iba1<sup>+</sup>DTR<sup>+</sup> microglia compared with all (DTR<sup>+</sup> and DTR<sup>-</sup>) microglia. Values normalized to those observed at 2 months. Two-way ANOVA: main effect of region,  $F_{(1,25)} = 2.7$ ,  $p = 0.11$ , n.s.; main effect of cell population,  $F_{(1,25)} = 3.6$ ,  $p = 0.07$ , n.s.; interaction,  $F_{(1,25)} = 0.89$ ,  $p = 0.35$ , n.s. **H**, Representative example of DTR<sup>+</sup> microglia exhibiting morphologic profile of cell division. \*\* $p < 0.0001$ .

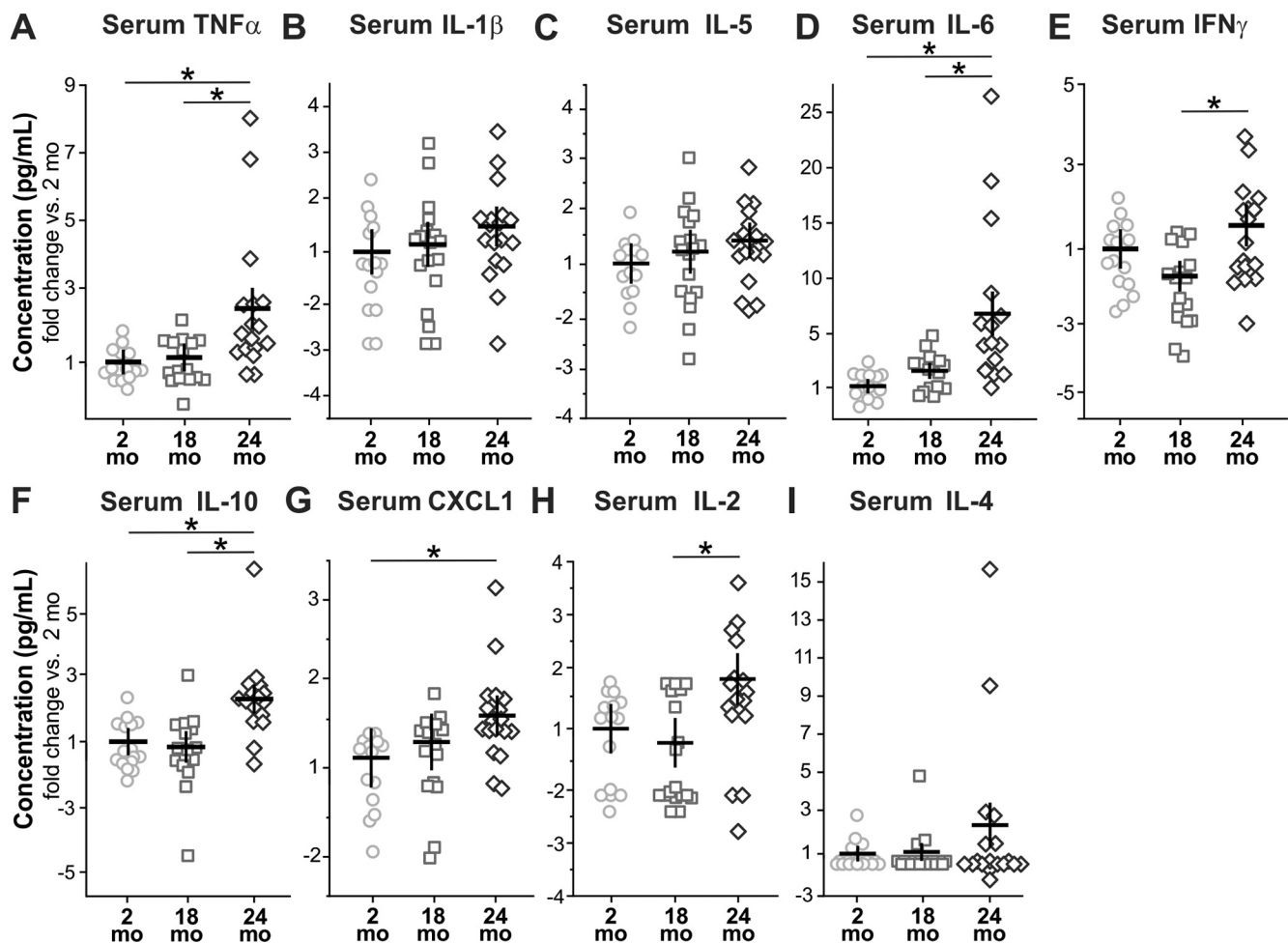


**Figure 7.** Systemic inflammation is not detectable in blood plasma until 22–24 months (mo) of age. **A**, Serum TNF $\alpha$ : one-way ANOVA,  $F_{(2,47)} = 10.14$ ,  $p = 0.0002$ . **B**, Serum IL-1 $\beta$ : one-way ANOVA,  $F_{(2,50)} = 2.32$ ,  $p = 0.11$ , n.s. **C**, Serum IL-5: one-way ANOVA,  $F_{(2,49)} = 1.44$ ,  $p = 0.25$ , n.s. \* $p < 0.05$ . **D**, Serum IL-6: one-way ANOVA,  $F_{(2,43)} = 9.15$ ,  $p = 0.0005$ . **E**, Serum IFN $\gamma$ : one-way ANOVA,  $F_{(2,49)} = 5.28$ ,  $p = 0.0085$ . **F**, Serum IL-10: one-way ANOVA,  $F_{(2,48)} = 10.16$ ,  $p = 0.0002$ . **G**, Serum chemokine ligand 1 (CXCL1, KC/GRO): one-way ANOVA,  $F_{(2,47)} = 4.23$ ,  $p = 0.021$ . **H**, Serum IL-2: one-way ANOVA,  $F_{(2,48)} = 4.92$ ,  $p = 0.011$ . **I**, Serum IL-4: one-way ANOVA,  $F_{(2,50)} = 1.44$ ,  $p = 0.25$ , n.s.

when pooling across the VTA and SNc (Fig. 9C,D). Collectively, these analyses suggest that neuron loss in the VTA/SNc is not extensive at the ages examined, in agreement with previous reports (Noda et al., 2020; Shaerzadeh et al., 2020), and that increases in VTA/SNc microglial proliferation and production of inflammatory factors likely precede rather than follow the beginnings of neuronal loss in these brain regions.

### Microglial ablation and repopulation suppress region-specific microglial aging responses

Microglia are dependent on activation of the colony stimulating factor 1 receptor (CSFR1) and can be ablated from the CNS via chronic pharmacological CSFR1 antagonism (Elmore et al., 2014). Subsequent removal of CSFR1 antagonism allows microglia to repopulate the CNS (Huang et al., 2018). Microglial ablation and repopulation in aging mice can partially reverse aging-induced changes observed in hippocampal and cortical microglia (Elmore et al., 2018; O’Neil et al., 2018), suggesting that cell-intrinsic factors shape microglial aging and that these factors can be “rejuvenated” or “reset” by ablation and repopulation. To probe whether cell-intrinsic factors contribute to early aging phenotypes of VTA microglia, we fed 13- to 20-month-old  $CX3CR1^{EGFP/+}$  mice diet containing the CSFR1 antagonist PLX5622 or control diet for 21 d. PLX5622

resulted in an  $91 \pm 0.2\%$  and  $84 \pm 1\%$  reduction in NAc and VTA microglia, respectively (Fig. 10A,B). Subsequent removal of PLX5622 for 21 d led to microglial repopulation in both regions. Within the NAc, microglial density in ablated/repopulated mice was comparable with that in control aged mice (Fig. 10B). Instead, in the VTA, microglial density in repopulated mice was significantly lower than that observed in control aged mice (Fig. 10B). Normalizing these values to the mean density observed in each region in 2-month-old mice revealed that in control 13- to 20-month-old mice, VTA microglial density was  $\sim 1.4$ -fold elevated (Fig. 10C), but in 13- to 20-month-old ablated/repopulated mice, it was equivalent to that observed in 2-month-old mice. These data support the idea that key cell-intrinsic factors may shape early aging responses of VTA microglia.

To gain additional insight into the local effects of microglial ablation/repopulation in the aging basal ganglia, we microdissected striatum (containing NAc) and midbrain (containing VTA) from control 3-month-old mice, control 13 to 20 month old (Aged CTR) mice, and 13 to 20 month old mice that had undergone PLX5622 microglial ablation and repopulation (Aged Repop) (Fig. 10D). qPCR analysis revealed that microglial ablation and repopulation modulated gene expression in both brain regions (Fig. 10E; Table 1), consistent with PLX5622 treatment

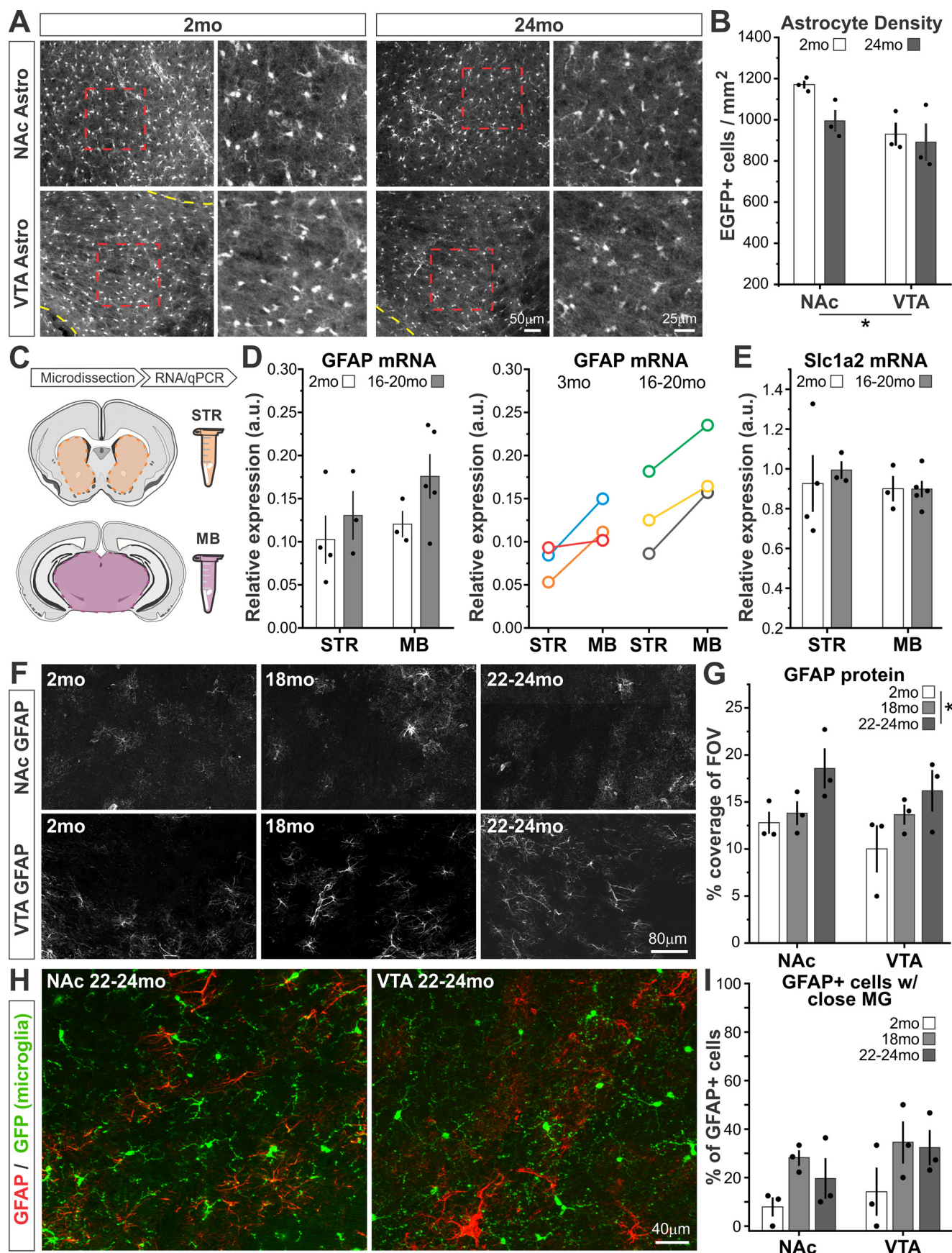


**Figure 8.** VTA microglial responses to aging are not accompanied by regional differences in astrocyte responses to aging. **A, B**, Images and quantification of NAc and VTA astrocyte density from 2 and 24 month (mo)-old *ALDH1L1-EGFP* mice. Dashed yellow line indicates VTA boundary. Two-way ANOVA: main effect of age,  $F_{(1,11)} = 3.2$ ,  $p = 0.11$ , n.s.; main effect of brain region,  $F_{(1,11)} = 8.1$ ,  $p = 0.02$ ; interaction,  $F_{(1,11)} = 1.3$ ,  $p = 0.29$ , n.s. **C**, Workflow schematic; midbrain (MB) and striatum (STR) were dissected from acute coronal forebrain sections followed by RNA

affecting microglia throughout the CNS. In general, microglial ablation and repopulation shifted tissue level gene expression in 13 to 20 month old mice back toward levels observed in 3-month-old mice. Levels of *Tnfa* and *IL-1 $\beta$*  showed trends toward increasing in both striatum and midbrain with aging, and these levels were reduced following ablation and repopulation (Fig. 10E,F). Genes associated with synaptic tagging and microglial elimination of synapses (*C1qa* and *Cr3*, respectively) were similarly elevated by aging and reduced by microglial ablation and repopulation (Fig. 10E,G). *Clec7a*, a marker of microglial reactivity, was elevated with aging, particularly in the midbrain, and these levels were reduced by microglial ablation and repopulation (Fig. 10E). Finally, genes associated with microglial lysosome function (*Cd68* and *Ctss*) showed trends toward increasing with aging and were reduced by microglial ablation and repopulation (Fig. 10E,H,I). Together, these results indicate that microglial ablation and repopulation normalize microglial density in the aging VTA/midbrain, at least temporarily, and suggest that normalized cell density is accompanied by a reduction in local inflammation and normalized microglial lysosome function. Moreover, these data raise the possibility that the local status of microglia during aging will be relevant for synapse integrity, consistent with studies showing that microglial ablation and repopulation can improve cognition in aging (Elmore et al., 2018).

### Exacerbated lysosome overload drives early aging responses of VTA microglia

Several observations highlight the potential importance of lysosome status as a cell-intrinsic factor that can shape microglial aging responses. CD68-filled somatic protrusions and cell process inclusions appeared to be more frequent in VTA microglia ( $5.6 \pm 2\%$  of cells) compared with NAc microglia ( $3.4 \pm 2\%$  of cells) (Fig. 2). Aging-induced increases in side scatter during FACS were more pronounced in midbrain microglia and were evident by 13 months of age (Fig. 3). Finally, microglial ablation and repopulation, which normalized VTA microglial density, modulated the abundance of *Cd68* and *Ctss* mRNA in the tissue (Fig. 10). Hence, we next sought to directly analyze microglial lysosomes to identify potential links between these organelles and the proliferative and inflammatory responses of VTA microglia during aging.

High-magnification confocal images of microglia in *CX3CR1<sup>EGFP/+</sup>* mice revealed that microglial lysosomes in 2-month-old mice were generally small and scattered

throughout the branching arbor of the cell. Instead, in 18-month-old mice, somatic lysosomes appeared enlarged and small lysosomes located in distal cell processes were fewer in number (Fig. 11A). To quantify these changes, we reconstructed both microglia and CD68<sup>+</sup> lysosomes in Imaris (Fig. 11B). Average lysosome size increased significantly in both the NAc and VTA between 2 and 13 months of age and increased further by 18 months of age in VTA microglia (Fig. 11C). Regional differences in the extent of lysosome swelling were also apparent when comparing the % volume of microglia occupied by lysosomes in the NAc and VTA of individual mice (Fig. 11D). At 2 months of age, lysosomes consistently occupied a smaller % volume of VTA microglia compared with NAc microglia in the same mouse. By 13 months of age, this regional difference had ceased to be significant; and at 18 months of age, the relationship was frequently the reverse, with a higher % of cell volume being occupied by lysosomes in the VTA. Finally, reductions in cell process lysosomes were significant in VTA microglia by 13 months of age and at 18 months of age exceeded the loss of cell process lysosomes observed in NAc microglia (Fig. 11E). These findings indicate that rearrangement of the lysosome network in VTA microglia is well-aligned with the time course of heightened proliferative and inflammatory responses of these cells during aging.

Given that microglial ablation and repopulation normalized microglial density in the VTA of aging mice, we sought to determine the local impact of ablation and repopulation on microglial lysosomes. While microglia in aged CTR mice frequently presented with enlarged somatic lysosomes, most microglia in aged Repop mice showed scattered smaller lysosomes, similar to lysosome networks observed in young adult mice (Fig. 11F). Quantitative analyses revealed that microglial ablation and repopulation significantly reduced the size of somatic lysosomes, and this reduction was larger in VTA microglia (Fig. 11G). In aged CTR mice, VTA microglia tended to have greater % cell volume occupied by lysosomes than NAc microglia from the same mice (Fig. 11H). In aged Repop mice instead, this interregional relationship was dampened. These findings further support potential links between lysosome status and VTA proliferative responses during aging.

RNAseq studies indicate that loss of the microglial fractalkine receptor (*CX3CR1*) results in premature aging profiles of microglia (Gyoneva et al., 2019). To continue to probe the relationship between microglial lysosome status and local microglial responses to aging, we analyzed lysosomes in *CX3CR1<sup>EGFP/+</sup>* (CX-Het) and *CX3CR1<sup>EGFP/EGFP</sup>* (CX-KO) mice (Fig. 11I). Focusing on 13 months of age, when increases in VTA microglial density and expression of TNF $\alpha$  first become apparent, this analysis revealed that average lysosome volume in VTA microglia from CX-KO mice significantly exceeded that of VTA microglia in CX-Het mice, as well as volume of lysosomes in NAc microglia from either genotype (Fig. 11J). In addition, loss of cell process lysosomes in VTA microglia of CX-KO mice exceeded that of NAc microglia, while this interregional trend had not yet reached significance in CX-Het mice at 13 months of age (Fig. 11K). These analyses indicate that lysosome rearrangements associated with aging are more severe in the VTA of *CX3CR1*-KO mice. To determine how this exacerbated lysosome rearrangement relates to proliferative responses of VTA microglia during aging, we quantified microglial cell density in C57Bl6 WT and CX-KO mice. In

←

extraction, and qPCR analysis. **D**, Left, Tissue levels of *Gfap* mRNA transcript in 2 and 16 to 20 month (mo) old *ALDH1L1-EGFP* mice. Two-way ANOVA: main effect of age,  $F_{(1,14)} = 2.5$ ,  $p = 0.14$ , n.s.; main effect of brain region,  $F_{(1,14)} = 1.4$ ,  $p = 0.26$ , n.s.; interaction,  $F_{(1,14)} = 0.27$ ,  $p = 0.62$ , n.s. Right, Comparison of *Gfap* transcript levels across region in individual mice. Data points from the same mice are the same color. **E**, Tissue levels of *Glt1* (*Sclt2*) mRNA transcript in 2 and 16 to 20 month old *ALDH1L1-EGFP* mice. Two-way ANOVA: main effect of age,  $F_{(1,14)} = 0.14$ ,  $p = 0.72$ , n.s.; main effect of brain region,  $F_{(1,14)} = 0.46$ ,  $p = 0.51$ , n.s.; interaction,  $F_{(1,14)} = 0.15$ ,  $p = 0.71$ , n.s. **F**, Representative images of GFAP immunostaining from the NAc and VTA of 2-, 18-, and 24-month-old *CX3CR1<sup>EGFP/+</sup>* mice. **G**, Quantification of GFAP immunostaining showing the percent coverage of the field of view (FOV) by GFAP<sup>+</sup> cells and processes. Two-way ANOVA: main effect of age,  $F_{(2,17)} = 5.5$ ,  $p = 0.02$ ; main effect of brain region,  $F_{(1,17)} = 1.4$ ,  $p = 0.26$ , n.s.; interaction,  $F_{(2,17)} = 0.3$ ,  $p = 0.74$ , n.s. **H**, Representative images showing spatial distribution of EGFP<sup>+</sup> microglia relative to GFAP<sup>+</sup> astrocytes. **I**, Percentage of GFAP<sup>+</sup> astrocytes with nearby microglia (<20  $\mu$ m). Two-way ANOVA: main effect of age,  $F_{(2,17)} = 4.1$ ,  $p = 0.04$ ; main effect of brain region,  $F_{(1,17)} = 2.0$ ,  $p = 0.18$ , n.s.; interaction,  $F_{(2,17)} = 0.13$ ,  $p = 0.88$ , n.s. \* $p < 0.05$ .



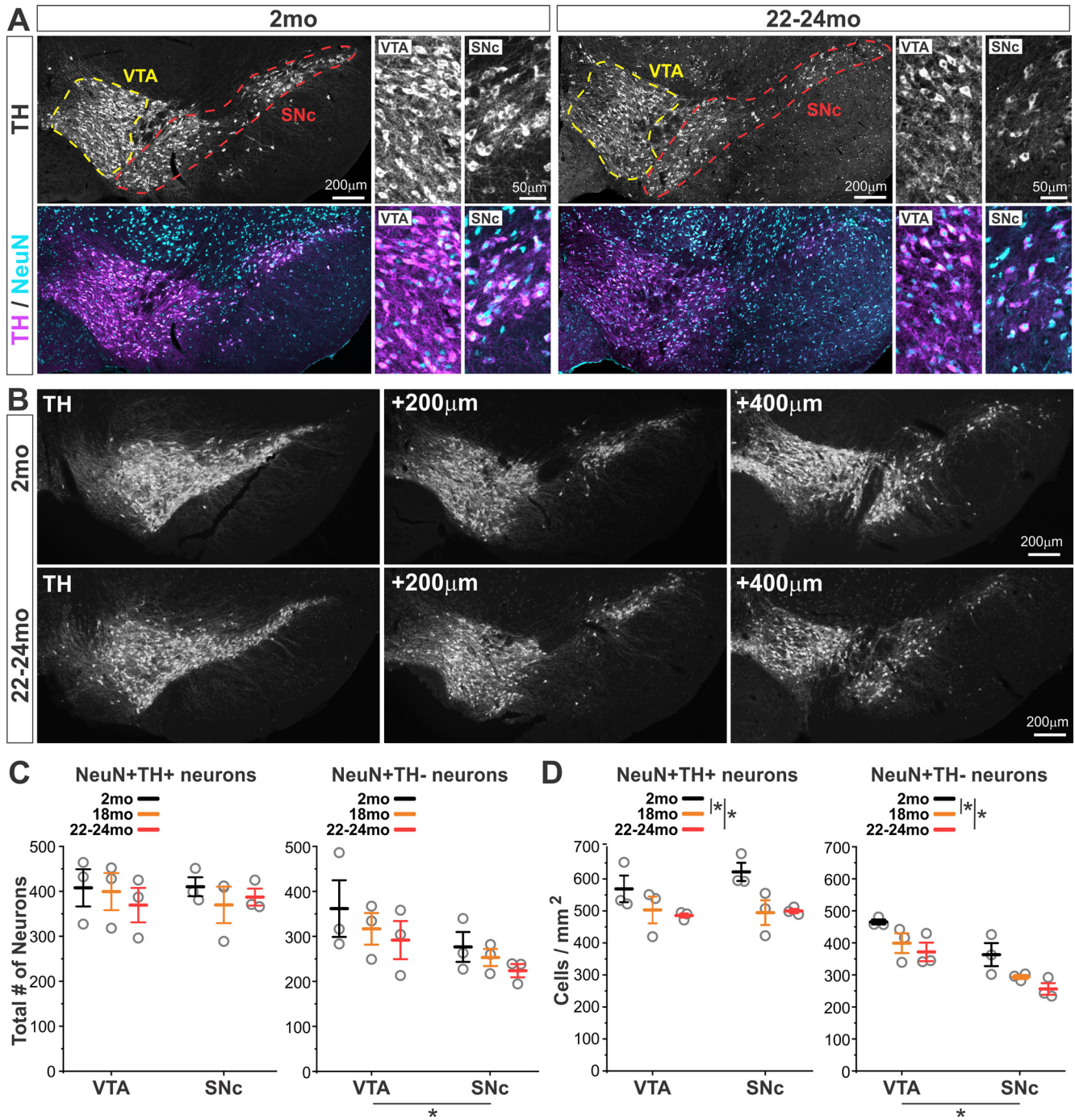


**Figure 9.** VTA and SNc microglial responses to aging are not accompanied by significant neuronal loss. **A**, Immunostaining for tyrosine hydroxylase (TH), which marks dopamine neurons, and NeuN, which labels all neurons, in 2- and 24-month (mo)-old *CX3CR1<sup>EGFP/+</sup>* mice. Yellow and red dashed lines indicate VTA and SNc divisions, respectively. Right panels, Higher-magnification images of VTA and SNc neurons. Background autofluorescence (lipofuscin) is visible throughout 24 month tissue but does not interfere with clear identification of neurons. **B**, Representative stereologically matched brain sections immunostained for TH from 2- and 24-month-old *CX3CR1<sup>EGFP/+</sup>* mice that were used for quantification of neuron abundance within the VTA and SNc. **C**, Total number of TH<sup>+</sup> neurons and TH<sup>-</sup> (non-dopaminergic) neurons across three stereologically matched brain sections during aging. Two-way ANOVAS: TH<sup>+</sup> neuron sum main effect of age,  $F_{(2,17)} = 43$ ,  $p = 0.66$ , n.s.; main effect of brain region,  $F_{(1,17)} = 0.01$ ,  $p = 0.92$ , n.s.; interaction,  $F_{(2,17)} = 0.24$ ,  $p = 0.79$ , n.s.; TH<sup>-</sup> neuron sum main effect of age,  $F_{(2,17)} = 1.31$ ,  $p = 0.30$ ; main effect of brain region,  $F_{(1,17)} = 5.4$ ,  $p = 0.04$ ; interaction,  $F_{(2,17)} = 0.04$ ,  $p = 0.96$ , n.s. **D**, Density of TH<sup>+</sup> neurons and TH<sup>-</sup> neurons during aging. Two-way ANOVAS: TH<sup>+</sup> neuron density main effect of age,  $F_{(2,17)} = 6.8$ ,  $p = 0.01$ ; main effect of brain region,  $F_{(1,17)} = 0.51$ ,  $p = 0.49$ , n.s.; interaction,  $F_{(2,17)} = 0.49$ ,  $p = 0.63$ , n.s.; TH<sup>-</sup> neuron density main effect of age,  $F_{(2,17)} = 8.97$ ,  $p = 0.004$ ; main effect of brain region,  $F_{(1,17)} = 29.64$ ,  $p = 0.0002$ ; interaction,  $F_{(2,17)} = 0.04$ ,  $p = 0.96$ , n.s. \* $p < 0.05$ .

WT mice, NAc microglial density did not change between 2 and 18 months, whereas VTA microglial density strongly trended toward increases at 18 months relative to 2 months (Fig. 1E). In CX-KO mice, NAc microglial density did not change between 2 and 18 months ( $341 \pm 12$  and  $360 \pm 12$  cells/mm<sup>2</sup>, respectively) and VTA microglial density was

significantly elevated compared with 2 months (2 months,  $225 \pm 11$  cells/mm<sup>2</sup>; 18 months,  $307 \pm 8$  cells/mm<sup>2</sup>). Normalizing cell densities observed at 18 months to those observed at 2 months for each genotype revealed that region-specific expansion of the microglial population is more severe in CK-KO mice (Fig. 11L). Collectively, these findings

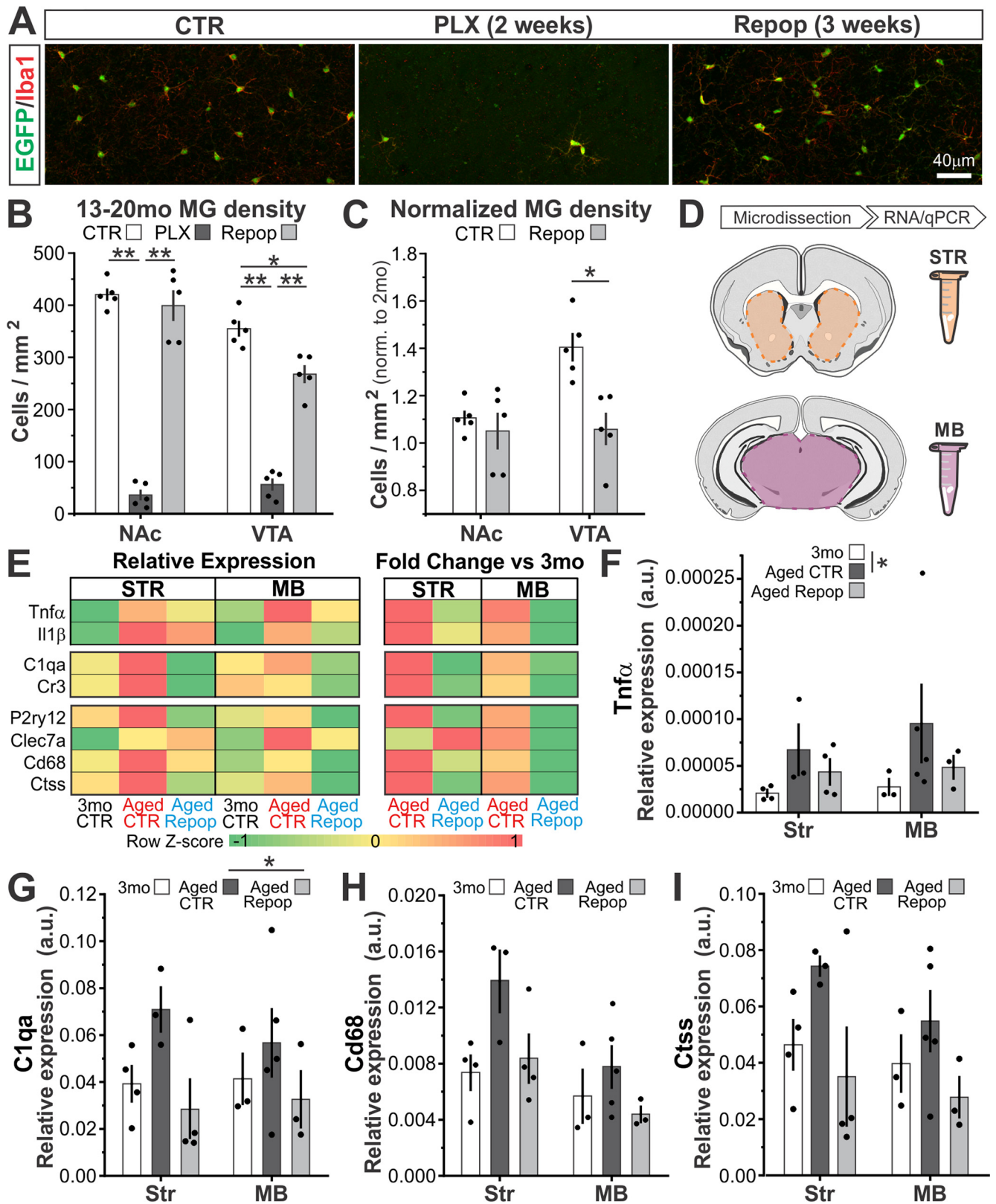


**Figure 10.** Region-specific microglial responses to aging are modulated by microglial ablation/repopulation. **A**, VTA microglia in 13–20 month (mo)  $CX3CR1^{EGFP/+}$  mice treated with control (CTR), Plexikon 5266 CSFR1 inhibitor diet (PLX), or PLX followed by control diet for 21 d to allow for microglial repopulation (Repop). **B**, Microglial density in 13–20 month  $CX3CR1^{EGFP/+}$  mice. Two-way ANOVA: main effect of treatment,  $F_{(2,29)} = 226.5$ ,  $p < 0.0001$ ; main effect of brain region,  $F_{(1,29)} = 17.4$ ,  $p = 0.0003$ ; interaction,  $F_{(2,29)} = 9.7$ ,  $p = 0.0008$ . **C**, Microglial density when normalized to 2 month values from each brain region and treatment. Two-way ANOVA: main effect of treatment,  $F_{(1,19)} = 10.5$ ,  $p = 0.005$ ; main effect of brain region,  $F_{(1,19)} = 6.17$ ,  $p = 0.02$ ; interaction,  $F_{(2,19)} = 5.5$ ,  $p = 0.03$ . **D**, Workflow schematic; striatum (STR) and midbrain (MB) were dissected from acute coronal forebrain sections followed by RNA extraction, and qPCR analysis. **E**, Heatmaps showing average expression level (left) and fold change compared with 3-month-old mice (right) for transcripts involved in local inflammation ( $Tnf\alpha$ ,  $Il1\beta$ ), microglial synaptic remodeling ( $C1qa$ ,  $Cr3$ ), and microglial functional state ( $P2ry12$ ,  $Clec7a$ ,  $Cd68$ ,  $Ctss$ ). Two-way ANOVAS for relative expression and fold change listed in Table 1. **F–I**, Scatterplots for subset of genes shown in **E**. \* $p < 0.05$ . \*\* $p < 0.0001$ .

**Table 1. Relative expression and fold change**

Gene	Data	Statistic	Group	Region	Interaction
<i>Tnf<math>\alpha</math></i>	Relative expression	<i>F</i>	5.66*	1.36	3.04
		<i>P</i>	0.017*	0.29	0.057
	Fold change	<i>F</i>	1.33	0.074	0.029
<i>Il1<math>\beta</math></i>	Relative expression	<i>F</i>	0.25	0.34	0.20
		<i>P</i>	0.78	0.72	0.93
	Fold change	<i>F</i>	1.01	0.42	0.23
<i>P2ry12</i>	Relative expression	<i>F</i>	2.74	1.94	1.79
		<i>P</i>	0.10	0.18	0.19
	Fold change	<i>F</i>	13.16**	0.61	0.27
<i>Cle7a</i>	Relative expression	<i>F</i>	5.88*	2.61	3.48*
		<i>P</i>	0.02*	0.11	0.39*
	Fold change	<i>F</i>	0.09	0.25	1.59
<i>Cd68</i>	Relative expression	<i>F</i>	0.77	0.63	0.23
		<i>P</i>	0.77	0.63	0.23
	Fold change	<i>F</i>	1.73	3.30	1.52
<i>Ctss</i>	Relative expression	<i>F</i>	0.22	0.07	0.25
		<i>P</i>	0.22	0.07	0.25
	Fold change	<i>F</i>	6.79*	2.20	0.057
<i>Ctqa</i>	Relative expression	<i>F</i>	0.024*	0.17	0.82
		<i>P</i>	0.024*	0.17	0.82
	Fold change	<i>F</i>	2.19	1.30	1.17
<i>Cr3</i>	Relative expression	<i>F</i>	0.15	0.31	0.37
		<i>P</i>	0.15	0.31	0.37
	Fold change	<i>F</i>	6.82*	0.24	0.082
<i>Cr3</i>	Relative expression	<i>F</i>	0.024*	0.64	0.78
		<i>P</i>	0.024*	0.64	0.78
	Fold change	<i>F</i>	3.69	−0.02	2.15
<i>Cr3</i>	Relative expression	<i>F</i>	0.054	—	0.091
		<i>P</i>	0.054	—	0.091
	Fold change	<i>F</i>	6.08*	0.32	0.56
<i>Cr3</i>	Relative expression	<i>F</i>	0.03*	0.58	0.47
		<i>P</i>	0.03*	0.58	0.47
	Fold change	<i>F</i>	1.93	−0.15	1.19
<i>Cr3</i>	Relative expression	<i>F</i>	0.18	—	0.36
		<i>P</i>	0.18	—	0.36
	Fold change	<i>F</i>	4.39	1.32	1.07
<i>Cr3</i>	Relative expression	<i>F</i>	0.06	0.27	0.323
		<i>P</i>	0.06	0.27	0.323

\**p* < 0.05. \*\**p* < 0.01.

suggest that regional differences in lysosome function and degradative demand placed on microglia are key drivers of region-specific responses of microglia to aging.

## Discussion

### Causes of microglial proliferation during aging

Here we demonstrate that the onset of microglial proliferation during aging varies widely and begins in midlife in select brain regions, such as the VTA/SNc. Microglia are highly proliferative during early postnatal development as they colonize the CNS (Ginhoux et al., 2013; Hope et al., 2020), after which they reach a steady state with minimal turnover in adulthood (Kierdorf and Prinz, 2017). Nonetheless, numerous stimuli cause microglia to mount substantial proliferative responses throughout the lifespan, including acute brain injury, disease processes, and repopulation after microglial ablation (Salter and Stevens, 2017; Wolf et al., 2017; Huang et al., 2018). During aging, microglial number in cortex (Tremblay et al., 2012; Hefendehl et al., 2014), hippocampus (Hovens et al., 2015), and CNS white matter tracts (Hart et al., 2012; Safaiyan et al., 2016) increases late in life (22–24 months in mice or rats). We find that, in the VTA and SNc, increases in microglial abundance can occur as early as middle age (13–14 months) (Fig. 1). The magnitude of microglial increases attained by late age in the VTA and SNc is much larger than that reported in cortex and on par with that reported in hippocampus and white matter. Moreover, by conditionally “tagging” microglia present in young

adulthood via expression of DTR, we show for the first time that local expansion of the microglial population is chiefly driven by proliferation of resident CNS microglia (Fig. 6). Others have reported no change or decreases in substantia nigra microglial number during aging (Hart et al., 2012; Sharaf et al., 2013; Shaerzadeh et al., 2020). However, exclusive reliance on Iba1 immunostaining, failure to distinguish SNc and substantia nigra pars reticulata, and use of 1 month time points as “young adult” comparisons complicate interpretation of these studies.

Causes of microglial proliferation during aging are less obvious than those in other contexts, such as populating the CNS during development, or clearing debris and dying cells after acute injury. Our findings argue that regional differences in microglial degradative capacity and/or regional differences in local degradative demand are linked to early expansion of the VTA/SNc microglial population. In young adulthood, VTA/SNc microglia have fewer lysosomes than microglia in other basal ganglia nuclei (De Biase et al., 2017), raising the possibility that they have reduced degradative capacity. Indeed, during aging, VTA microglia exhibit more severe lysosome swelling and loss of cell process lysosomes than NAc microglia (Fig. 11). The time course of these lysosome rearrangements is tightly correlated with the time course of VTA microglial proliferation and production of inflammatory factors during aging. Moreover, microglial ablation and repopulation during early aging significantly normalized lysosome size in VTA microglia and reduced VTA microglial density to young adult levels (Figs. 10 and 11). In contrast, CX3CR1 KO exacerbated VTA microglial lysosome swelling and further elevated VTA microglial density increases during aging (Fig. 11). These data highlight a key relationship between the status of these organelles and microglial functional state. Future studies that analyze microglial lysosome pH, the complement of hydrolases present in microglial lysosomes, and that include genetic manipulation of microglial lysosome function can further elucidate how these organelles regulate microglial aging responses.

Although we did not detect substantial neuron cell death in the VTA/SNc (Fig. 9) at ages when microglia begin to proliferate and produce inflammatory factors, this does not preclude that other changes in neuronal function during aging also play a key role in promoting microglial aging responses. Age-dependent decline in dopamine-dependent cognition and movement is observed in humans (Visser and Bloem, 2005; Bäckman et al., 2010; Chowdhury et al., 2013; Sarter et al., 2014), nonhuman primates (Siddiqi et al., 1999), and rodents (Shoji et al., 2016; Noda et al., 2020), supporting the idea of altered neuronal function within this circuitry. Microglia are equipped to sense and respond to changes in ongoing neuronal activity (Badimon et al., 2020; Cserép et al., 2020), and increases in cortical microglial number during aging were modulated by loss of sensory input (Tremblay et al., 2012). Future studies can explore the impact of changing patterns of neuronal activity within the VTA/SNc on microglial proliferation and inflammatory responses. Additional features of dopamine neurons also merit investigation in future studies. Dopamine synthetic pathways lead to elevated free radical production by these neurons (Brichta and Greengard, 2014; Fu et al., 2018), and they can release prostaglandins in pathologic contexts (Ikeda-Matsuo et al., 2021). Defining relationships between local free radical production, prostaglandin signaling, and VTA/SNc microglial proliferation and inflammatory factor

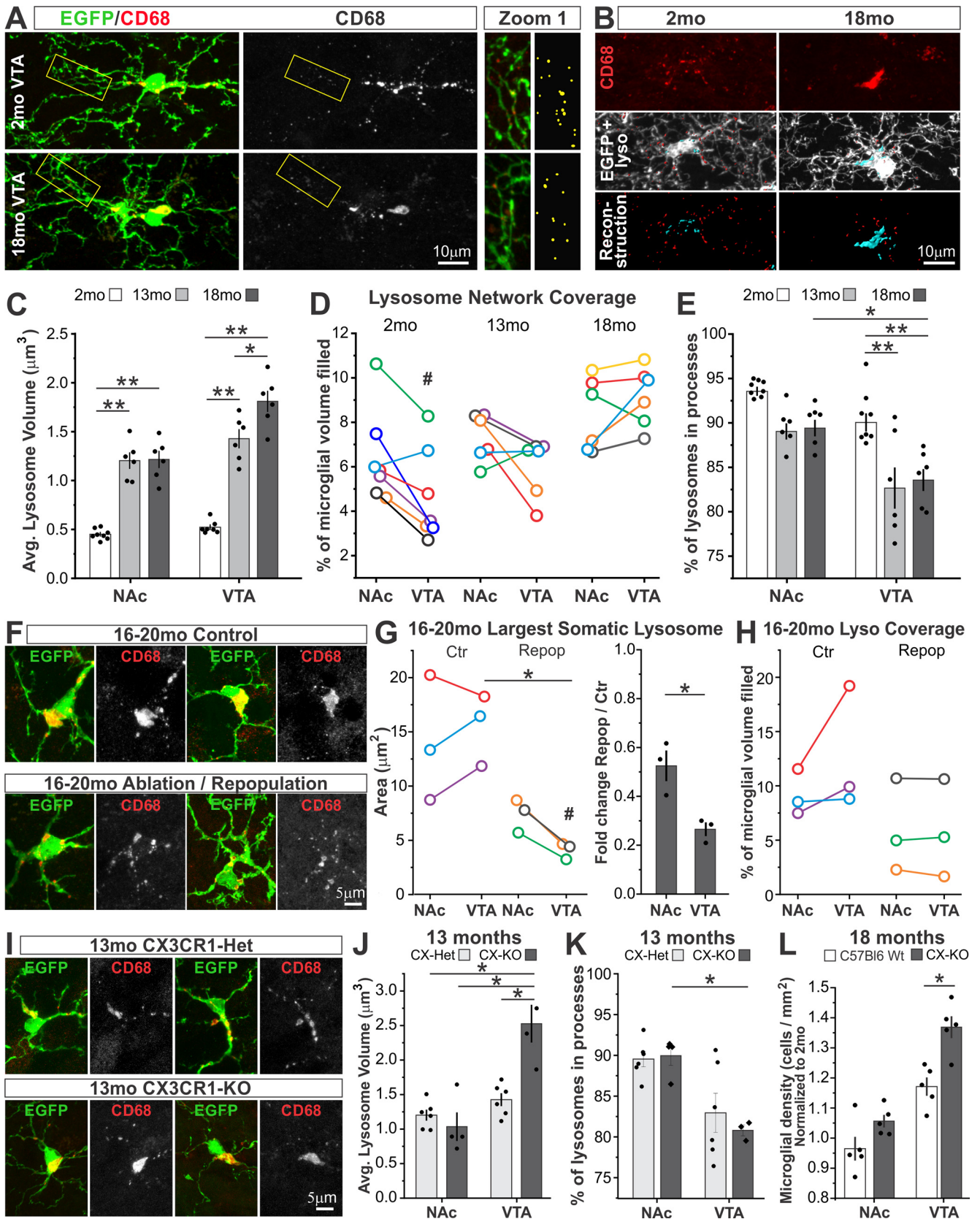


**Figure 11.** Microglial lysosome status is tightly aligned with early VTA microglial aging responses. **A**, Representative high-magnification confocal images of VTA microglia (EGFP) and microglial lysosomes (CD68) in 2 and 18 months (mo) in *CX3CR1<sup>EGFP/+</sup>* mice. Yellow boxes represent distal microglial processes where the location of lysosomes is tagged by yellow dots at right. **B**, Representative examples of 3D reconstruction of microglial lysosomes in 2- and 18-month-old *CX3CR1<sup>EGFP/+</sup>* mice. Cyan represents somatic lysosomes. Red represents cell process lysosomes in reconstruction. **C**, Quantification of average lysosome size in microglia during aging. Two-way ANOVA: main effect of age,  $F_{(2,38)} = 130.1, p < 0.0001$ ; main effect of brain region,  $F_{(1,38)} = 27.0, p < 0.0001$ ; interaction,  $F_{(2,38)} = 7.5, p = 0.002$ . **D**, Degree to which the lysosome network fills microglial cells at different ages. Two-way ANOVA: main effect of age,  $F_{(2,37)} = 10.5, p = 0.0003$ ; main effect of brain region,  $F_{(1,37)} = 1.22, p = 0.28, n.s.$ ; interaction,  $F_{(2,37)} = 1.5, p = 0.23, n.s.$  **E**, Loss of cell process lysosomes during aging quantified as the % of all lysosomes found in cell

production will shed additional light on factors that shape region-specific microglial aging responses.

### Chronic local inflammation as one consequence of microglial proliferation during aging?

During aging, increases in systemic and CNS inflammation have been observed across species (Lucin and Wyss-Coray, 2009; Cunningham, 2013; Lecours et al., 2018). We show that CNS inflammation during aging is not uniform; VTA (and likely SNc) neurons are exposed to chronic low-level inflammation throughout the lifespan with regional differences accentuating with age (Fig. 4). Although we cannot unequivocally pinpoint the source of local inflammation, several observations suggest that microglia play a central role in regulating local inflammatory milieu during aging. First, the time course of VTA microglial proliferation is tightly aligned with the time course of increasing levels of *Tnfa* and *IL-1β* transcript in this brain region. Furthermore, region-specific, age-associated increases in *Tnfa* transcript were observed within midbrain microglia as early as 13 months of age (Fig. 3). Finally, published transcriptome data from aging astrocytes suggest that *Tnfa* and *IL-1β* are not highly expressed by these cells in young or aged mice (Orre et al., 2014; Boisvert et al., 2018). In addition, we did not observe increases in astrocyte density during aging, GFAP transcript and protein did not differ across NAc and VTA, and subtle increases in GFAP protein did not reach significance until 22–24 months of age (Fig. 8). Astrocyte expression of numerous genes does change during aging in a region-specific manner (Boisvert et al., 2018), and our data do not preclude that astrocytes shape how neuroprotective or neurotoxic the local environment is during aging. However, our findings argue that microglia are likely to be the main source of local VTA/SNc inflammation that emerges in midlife.

The aging-induced increases in inflammation that we report are likely well below those experienced during active degenerative disease. Consistent with this idea, we observe relatively little VTA and SNc neuronal loss by 18 and 22–24 months of age (Fig. 9). However, synapse loss and synapse dysfunction rather than overt neuronal death are most tightly linked to cognitive deficits during aging and presymptomatic stages of neurodegenerative disease (Burke and Barnes, 2006; Bell and Hardingham, 2011; Morrison and Baxter, 2012; Bellucci et al., 2016). Several

observations suggest that perturbed synaptic function is a likely outcome of early, mild elevations in inflammation within the VTA/SNc. Age-dependent decline in dopamine-dependent cognition and movement is observed in humans (Visser and Bloem, 2005; Bäckman et al., 2010; Chowdhury et al., 2013; Sarter et al., 2014), nonhuman primates (Siddiqi et al., 1999), and rodents (Shoji et al., 2016; Noda et al., 2020), supporting the idea of perturbed synaptic function within this circuitry. The cytokines we find to be elevated within the VTA,  $TNF\alpha$  and  $IL-1\beta$ , have both been shown to influence key aspects of glutamatergic and GABAergic synapse receptor composition, function, and plasticity (Prieto and Cotman, 2017; Heir and Stellwagen, 2020). We also found that genes associated with synaptic tagging and microglial elimination of synapses (*C1qa* and *Cr3*, respectively) were elevated by 16–20 months in the midbrain (Fig. 10). Finally, lifestyle manipulations that alter microglial phenotype and reduce inflammation are correlated with improved cognition during aging (Newcombe et al., 2018; Walker et al., 2019).

### How do region-specific responses of microglia to aging relate to disease susceptibility?

Although we do not observe significant dopamine neuron death during aging, several observations suggest that changing microglial attributes and chronic local inflammation in the VTA and SNc could contribute to increased disease susceptibility of dopamine neurons (Brichta and Greengard, 2014; Fu et al., 2018). First, epidemiological studies indicate that long-term use of non-steroidal anti-inflammatory medication reduced the risk of Alzheimer's and Parkinson's disease (PD) by almost 50% (McGeer et al., 1996; Chen et al., 2005; Gagne and Power, 2010), suggesting that the local inflammatory milieu during aging does shape disease susceptibility. Second, accumulation of aggregate-prone proteins, such as  $\alpha$ -synuclein, is linked to risk of degenerative disease (Soto and Pritzkow, 2018). Microglia can phagocytose  $\alpha$ -synuclein and degrade it via lysosomes or transfer it to other microglia via tunneling nanotubes (Choi et al., 2020; Scheiblich et al., 2021). Significant reductions in microglial cell process branching in VTA by 18 months (Fig. 2) and more severe lysosome swelling (Fig. 11), which impairs overall membrane recycling and associated cell process motility and phagocytosis (Xu and Ren, 2015; Lie and Nixon, 2019; Ballabio and Bonifacino, 2020; de Araujo et al., 2020), suggest that VTA microglial capacity to support aggregate clearance will likely be reduced by late middle age. Finally, microglia respond to many of the environmental risk factors that increase PD susceptibility, including traumatic brain injury and exposure to toxins (Ransohoff and Perry, 2009; Taetzsch and Block, 2013; Hanamsagar and Bilbo, 2017). Together, these observations suggest that early changes in VTA and SNc microglia during aging lay a foundation for heightened vulnerability for nearby dopamine neurons that will intersect with other genetic and environmental risk factors to determine overall disease risk.

Two other factors that shape disease risk should be mentioned. First, men are at higher risk of developing PD than women (Wooten et al., 2004). Although male-female differences in microglial aging have been reported (Lenz et al., 2013; Kopec et al., 2018; VanRyzin et al., 2019), we did not observe any obvious male-female differences in the region-specific microglial changes that we report here (Fig. 12). Further research would be needed to unequivocally determine whether sex influences the degree of region-specific microglial responses to aging. Second,

←

processes. Two-way ANOVA: main effect of age,  $F_{(2,39)} = 15.1$ ,  $p < 0.0001$ ; main effect of brain region,  $F_{(1,39)} = 27.0$ ,  $p < 0.0001$ ; interaction,  $F_{(2,39)} = 1.17$ ,  $p = 0.32$ , n.s. **F**, Representative images of somatic and proximal process lysosomes in aging CTR and microglial ablation/repopulation (Repop) mice. **G**, Quantification of largest somatic lysosomes in CTR and Repop mice. Two-way ANOVA for area: main effect of brain region,  $F_{(1,11)} = 0.22$ ,  $p = 0.65$ , n.s.; main effect of treatment,  $F_{(1,11)} = 20.8$ ,  $p = 0.002$ ; interaction,  $F_{(1,11)} = 1.4$ ,  $p = 0.27$ , n.s. **H**, Degree to which the lysosome network fills microglial cells. Two-way ANOVA: main effect of brain region,  $F_{(1,11)} = 0.44$ ,  $p = 0.53$ , n.s.; main effect of treatment,  $F_{(1,11)} = 3.9$ ,  $p = 0.08$ , n.s.; interaction,  $F_{(1,11)} = 0.51$ ,  $p = 0.49$ , n.s. **I**, Representative images of somatic and proximal process lysosomes in 13-month-old  $CX3CR1^{EGFP/+}$  (CX-Het) mice and  $CX3CR1^{EGFP/EGFP}$  (CX-KO) mice. **J**, Quantification of average lysosome size in microglia from 13-month-old CX-Het and CX-KO mice. Two-way ANOVA: main effect of region,  $F_{(1,18)} = 27.6$ ,  $p < 0.0001$ ; main effect of genotype,  $F_{(1,18)} = 6.5$ ,  $p = 0.02$ ; interaction,  $F_{(1,18)} = 13.7$ ,  $p = 0.002$ . **K**, Loss of cell process lysosomes in 13-month-old CX-Het and CX-KO mice quantified as the % of all lysosomes found in cell processes. Two-way ANOVA: main effect of region,  $F_{(1,18)} = 18.6$ ,  $p = 0.0006$ ; main effect of genotype,  $F_{(1,18)} = 0.22$ ,  $p = 0.64$ , n.s.; interaction,  $F_{(1,18)} = 0.05$ ,  $p = 0.45$ , n.s. **L**, Microglial density during aging in C57Bl6 WT and CX-KO mice. Values normalized to 2 month values from each brain region and genotype. Two-way ANOVA: main effect of genotype,  $F_{(1,16)} = 18.9$ ,  $p = 0.0005$ ; main effect of brain region,  $F_{(1,16)} = 63.4$ ,  $p < 0.0001$ ; interaction,  $F_{(2,16)} = 2.6$ ,  $p = 0.12$ , n.s. \* $p < 0.05$ ; \*\* $p < 0.0001$ ; † $p < 0.05$ ; paired *t* test.

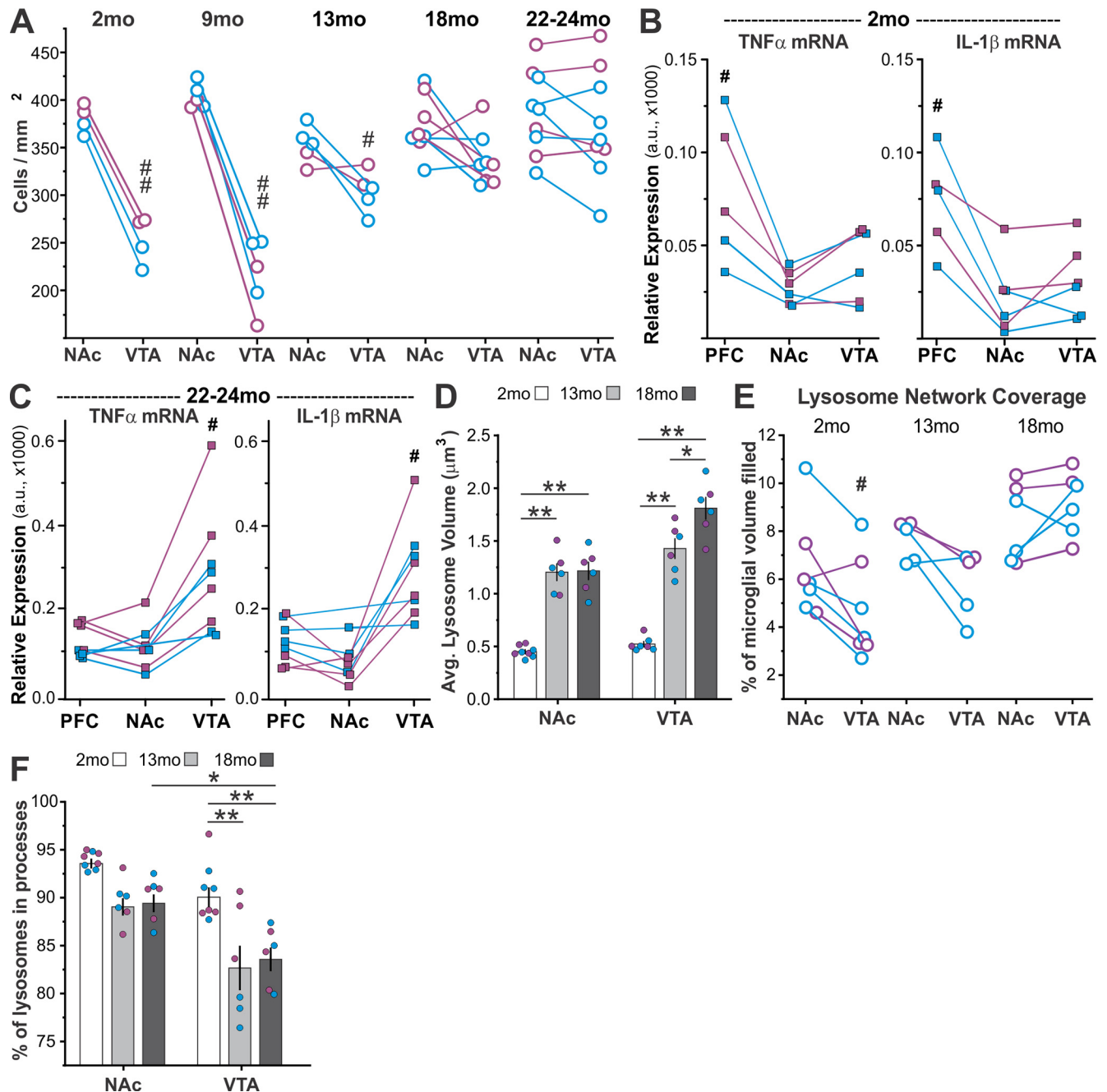


**Figure 12.** Prominent male-female differences are not observed in region-specific responses of basal ganglia microglia to aging. **A**, Graph of microglial cell density in the aging VTA and NAc from Figure 1D. Blue represents male mice. Purple represents female mice. **B**, **C**, Graphs of *TNF $\alpha$*  and *IL-1 $\beta$*  transcript in the VTA and NAc of 2 and 22 to 24 month (mo) old mice from Figure 4C. Blue represents male mice. Purple represents female mice. **D–F**, Graphs of average lysosome size, lysosome coverage of microglia, and loss of cell process lysosomes from Figure 11C–E. Blue represents male mice. Purple represents female mice.

SNc dopamine neurons are more vulnerable to PD than VTA dopamine neurons, although both are eventually lost as disease progresses (Brichta and Greengard, 2014; Fu et al., 2018). VTA and SNc microglia are much more similar to one another than they are to microglia in other basal ganglia nuclei or cortex (De Biase et al., 2017). VTA and SNc microglial responses to aging were also very similar in terms of increasing cell density, increases in tissue coverage, somatic CD68<sup>+</sup> protrusions, and cell process inclusions (Fig. 5). However, microglial “clusters” among and adjacent to dopamine neurons appeared to be larger in the SNc than in VTA. These microglia clusters resemble multinucleated giant cells (MGCs) that have been reported in

the context of presymptomatic amyotrophic lateral sclerosis (Fendrick et al., 2007), HIV-induced dementia (Naito et al., 1989), macaque and rat models of PD (Lecours et al., 2018), and in white matter tracts of aged (21 months) mice (Hart et al., 2012). Similar to our observations in the aging VTA/SNc, these studies report that MGCs rarely contained obvious pyknotic nuclei and that they tended to be arranged in circular fashion with nuclei around the periphery. There were no obvious differences between dopamine neurons near to these clusters and more distant from these clusters. *In vitro* experiments suggest that microglial MGCs are 2- to 4-fold more phagocytic and that their formation can be induced by stimulation with phagocytic

challenges, such as by amyloid- $\beta$  and  $\alpha$ -synuclein, as well as by inflammatory stimuli, such as LPS, TNF $\alpha$ , and IFN $\gamma$  (Hornik et al., 2014). While there is still little information available about microglial MGCs *in vivo*, if these structures are larger in the SNc, this could point to greater inflammatory signaling, phagocytic demand, and/or elevated  $\alpha$ -synuclein than other nearby regions, including the VTA. Additional research will be needed to determine whether this is the case and whether subtle differences in VTA and SNc microglial responses to aging further elevate the vulnerability of SNc dopamine neurons.

## References

- Ayata P, Badimon A, Strasburger HJ, Duff MK, Montgomery SE, Loh YH, Ebert A, Pimenova AA, Ramirez BR, Chan AT, Sullivan JM, Purushothaman I, Scarpa JR, Goate AM, Busslinger M, Shen L, Losic B, Schaefer A (2018) Epigenetic regulation of brain region-specific microglia clearance activity. *Nat Neurosci* 21:1049–1060.
- Bäckman L, Lindenberger U, Li SC, Nyberg L (2010) Linking cognitive aging to alterations in dopamine neurotransmitter functioning: recent data and future avenues. *Neurosci Biobehav Rev* 34:670–677.
- Badimon A, et al. (2020) Negative feedback control of neuronal activity by microglia. *Nature* 586:417–423.
- Ballabio A, Bonifacino JS (2020) Lysosomes as dynamic regulators of cell and organismal homeostasis. *Nat Rev Mol Cell Biol* 21:101–118.
- Baufeld C, O’Loughlin E, Calcagno N, Madore C, Butovsky O (2018) Differential contribution of microglia and monocytes in neurodegenerative diseases. *J Neural Transm (Vienna)* 125:809–826.
- Bell KF, Hardingham GE (2011) The influence of synaptic activity on neuronal health. *Curr Opin Neurobiol* 21:299–305.
- Bellucci A, Mercuri NB, Venneri A, Faustini G, Longhena F, Pizzi M, Missale C, Spano P (2016) Parkinson’s disease: from synaptic loss to connectome dysfunction. *Neuropathol Appl Neurobiol* 42:77–94.
- Boisvert MM, Erikson GA, Shokhirev MN, Allen NJ (2018) The aging astrocyte transcriptome from multiple regions of the mouse brain. *Cell Rep* 22:269–285.
- Brichta L, Greengard P (2014) Molecular determinants of selective dopaminergic vulnerability in Parkinson’s disease: an update. *Front Neuroanat* 8:152.
- Burke SN, Barnes CA (2006) Neural plasticity in the ageing brain. *Nat Rev Neurosci* 7:30–40.
- Burns JC, Cotleur B, Walther DM, Bajrami B, Rubino SJ, Wei R, Franchimont N, Cotman SL, Ransohoff RM, Mingueneau M (2020) Differential accumulation of storage bodies with aging defines discrete subsets of microglia in the healthy brain. *Elife* 9:e57495.
- Chen H, Jacobs E, Schwarzschild MA, McCullough ML, Calle EE, Thun MJ, Ascherio A (2005) Nonsteroidal antiinflammatory drug use and the risk for Parkinson’s disease. *Ann Neurol* 58:963–967.
- Choi I, Zhang Y, Seegobin SP, Pruvost M, Wang Q, Purtell K, Zhang B, Yue Z (2020) Microglia clear neuron-released  $\alpha$ -synuclein via selective autophagy and prevent neurodegeneration. *Nat Commun* 11:1386.
- Chowdhury R, Guitart-Masip M, Lambert C, Dayan P, Huys Q, Düzel E, Dolan RJ (2013) Dopamine restores reward prediction errors in old age. *Nat Neurosci* 16:648–653.
- Clarke LE, Liddelow SA, Chakraborty C, Münch AE, Heiman M, Barres BA (2018) Normal aging induces A1-like astrocyte reactivity. *Proc Natl Acad Sci USA* 115:E1896–E1905.
- Cserép C, et al. (2020) Microglia monitor and protect neuronal function through specialized somatic purinergic junctions. *Science* 367:528–537.
- Cunningham C (2013) Microglia and neurodegeneration: the role of systemic inflammation. *Glia* 61:71–90.
- Damani MR, Zhao L, Fontainhas AM, Amaral J, Fariss RN, Wong WT (2011) Age-related alterations in the dynamic behavior of microglia. *Aging Cell* 10:263–276.
- de Araujo ME, Liebscher G, Hess MW, Huber LA (2020) Lysosomal size matters. *Traffic* 21:60–75.
- De Biase LM, Schuebel KE, Fusedel ZH, Jair K, Hawes IA, Cimbri R, Zhang HY, Liu QR, Shen H, Xi ZX, Goldman D, Bonci A (2017) Local cues establish and maintain region-specific phenotypes of basal ganglia microglia. *Neuron* 95:341–356.
- de Haas AH, Boddeke HW, Biber K (2008) Region-specific expression of immunoregulatory proteins on microglia in the healthy CNS. *Glia* 56:888–894.
- DiSabato DJ, Quan N, Godbout JP (2016) Neuroinflammation: the devil is in the details. *J Neurochem* 139:136–153.
- Elmore MR, Najafi AR, Koike MA, Dagher NN, Spangenberg EE, Rice RA, Kitazawa M, Matusow B, Nguyen H, West BL, Green KN (2014) CSF1 receptor signaling is necessary for microglia viability, which unmasks a cell that rapidly repopulates the microglia-depleted adult brain. *Neuron* 82:380–397.
- Elmore MR, Hohsfield LA, Kramár EA, Soreq L, Lee RJ, Pham ST, Najafi AR, Spangenberg EE, Wood MA, West BL, Green KN (2018) Replacement of microglia in the aged brain reverses cognitive, synaptic, and neuronal deficits in mice. *Aging Cell* 17:e12832.
- Fendrick SE, Xue QS, Streit WJ (2007) Formation of multinucleated giant cells and microglial degeneration in rats expressing a mutant Cu/Zn superoxide dismutase gene. *J Neuroinflammation* 4:9.
- Fu H, Hardy J, Duff KE (2018) Selective vulnerability in neurodegenerative diseases. *Nat Neurosci* 21:1350–1358.
- Gagne JJ, Power MC (2010) Anti-inflammatory drugs and risk of Parkinson disease: a meta-analysis. *Neurology* 74:995–1002.
- Ginhoux F, Lim S, Hoeffel G, Low D, Huber T (2013) Origin and differentiation of microglia. *Front Cell Neurosci* 7:45.
- Grabert K, Michael T, Karavolos MH, Clohisey S, Baillie JK, Stevens MP, Freeman TC, Summers KM, McColl BW (2016) Microglial brain region-dependent diversity and selective regional sensitivities to aging. *Nat Neurosci* 19:504–516.
- Gunner G, Cheadle L, Johnson KM, Ayata P, Badimon A, Mondo E, Nagy MA, Liu L, Bemiller SM, Kim KW, Lira SA, Lamb BT, Tapper AR, Ransohoff RM, Greenberg ME, Schaefer A, Schafer DP (2019) Sensory lesioning induces microglial synapse elimination via ADAM10 and fractalkine signaling. *Nat Neurosci* 22:1075–1088.
- Gyoneva S, Hosur R, Gosselin D, Zhang B, Ouyang Z, Cotleur AC, Peterson M, Allaire N, Challa R, Cullen P, Roberts C, Miao K, Reynolds TL, Glass CK, Burkly L, Ransohoff RM (2019) Cx3cr1-deficient microglia exhibit a premature aging transcriptome. *Life Sci Alliance* 2:e201900453.
- Hammond TR, Dufort C, Dissing-Olesen L, Giera S, Young A, Wysoker A, Walker AJ, Gergits F, Segel M, Nemesh J, Marsh SE, Saunders A, Macosko E, Ginhoux F, Chen J, Franklin RJ, Piao X, McCarroll SA, Stevens B (2019) Single-cell RNA sequencing of microglia throughout the mouse lifespan and in the injured brain reveals complex cell-state changes. *Immunity* 50:253–271.
- Hanamsagar R, Bilbo SD (2017) Environment matters: microglia function and dysfunction in a changing world. *Curr Opin Neurobiol* 47:146–155.
- Hart AD, Wyttenbach A, Perry VH, Teeling JL (2012) Age related changes in microglial phenotype vary between CNS regions: grey versus white matter differences. *Brain Behav Immun* 26:754–765.
- Hayashi Y, Koyanagi S, Kusunose N, Takayama F, Okada R, Wu Z, Ohdo S, Nakanishi H (2013) Diurnal spatial rearrangement of microglial processes through the rhythmic expression of P2Y12 receptors. *J Neurol Disord* 1:2.
- Hefendehl JK, Neher JJ, Sühs RB, Kohsaka S, Skodras A, Jucker M (2014) Homeostatic and injury-induced microglia behavior in the aging brain. *Aging Cell* 13:60–69.
- Heir R, Stellwagen D (2020) TNF-mediated homeostatic synaptic plasticity: from *in vitro* to *in vivo* models. *Front Cell Neurosci* 14:565841.
- Hickman S, Izzy S, Sen P, Morsett L, El Khoury J (2018) Microglia in neurodegeneration. *Nat Neurosci* 21:1359–1369.
- Hong S, Beja-Glasser VF, Nfonoyim BM, Frouin A, Li S, Ramakrishnan S, Merry KM, Shi Q, Rosenthal A, Barres BA, Lemere CA, Selkoe DJ, Stevens B (2016) Complement and microglia mediate early synapse loss in Alzheimer mouse models. *Science* 352:712–716.
- Hope KT, Hawes IA, Moca EN, Bonci A, De Biase LM (2020) Maturation of the microglial population varies across mesolimbic nuclei. *Eur J Neurosci* 52:3689–3709.
- Hornik TC, Neniskyte U, Brown GC (2014) Inflammation induces multinucleation of microglia via PKC inhibition of cytokinesis, generating highly phagocytic multinucleated giant cells. *J Neurochem* 128:650–661.
- Hovens IB, van Leeuwen BL, Nyakas C, Heineman E, van der Zee EA, Schoemaker RG (2015) Postoperative cognitive dysfunction and microglial activation in associated brain regions in old rats. *Neurobiol Learn Mem* 118:74–79.

- Huang Y, Xu Z, Xiong S, Sun F, Qin G, Hu G, Wang J, Zhao L, Liang YX, Wu T, Lu Z, Humayun MS, So KF, Pan Y, Li N, Yuan TF, Rao Y, Peng B (2018) Repopulated microglia are solely derived from the proliferation of residual microglia after acute depletion. *Nat Neurosci* 21:530–540.
- Ikeda-Matsuo Y, Yunoki N, Kaji M, Uematsu S, Akira S, Takahashi T, Tanabe M (2021) Microsomal prostaglandin E synthase-1 induced by hemoglobin in microglia contributes to inflammation and neuronal death. *Proc Annu Meet Japanese Pharmacol Soc* 94:1–14.
- Kennedy RH, Silver R (2015) Neuroimmune signaling: cytokines and the CNS. In: *Neuroscience in the 21st Century*. New York:Springer.
- Kierdorf K, Prinz M (2017) Microglia in steady state. *J Clin Invest* 127:2301–3209.
- Kopec AM, Smith CJ, Ayre NR, Sweat SC, Bilbo SD (2018) Microglial dopamine receptor elimination defines sex-specific nucleus accumbens development and social behavior in adolescent rats. *Nat Commun* 9:3769.
- Lecours C, Bordeleau M, Cantin L, Parent M, di Paolo T, Tremblay MÈ (2018) Microglial implication in Parkinson's disease: loss of beneficial physiological roles or gain of inflammatory functions? *Front Cell Neurosci* 12:282.
- Lenz KM, Nugent BM, Haliyur R, McCarthy MM (2013) Microglia are essential to masculinization of brain and behavior. *J Neurosci* 33:2761–2772.
- Liddelow SA, et al. (2017) Neurotoxic reactive astrocytes are induced by activated microglia. *Nature* 541:481–487.
- Lie PP, Nixon RA (2019) Lysosome trafficking and signaling in health and neurodegenerative diseases. *Neurobiol Dis* 122:94–105.
- Lu T, Pan Y, Kao SY, Li C, Kohane I, Chan J, Yankner BA (2004) Gene regulation and DNA damage in the ageing human brain. *Nature* 429:883–891.
- Lucin KM, Wyss-Coray T (2009) Immune activation in brain aging and neurodegeneration: too much or too little? *Neuron* 64:110–122.
- McGeer PL, Schulzer M, McGeer EG (1996) Arthritis and anti-inflammatory agents as possible protective factors for Alzheimer's disease: a review of 17 epidemiologic studies. *Neurology* 47:425–432.
- Morales M, Margolis EB (2017) Ventral tegmental area: cellular heterogeneity, connectivity and behaviour. *Nat Rev Neurosci* 18:73–85.
- Morrison JH, Baxter MG (2012) The ageing cortical synapse: hallmarks and implications for cognitive decline. *Nat Rev Neurosci* 13:240–285.
- Naito M, Jogasaki M, Takahashi K, Matsumi S, Hattori T, Takatsuki K (1989) Ultrastructural behavior of human immunodeficiency virus (HIV) in multinucleated giant cells in the brain of a Japanese hemophilic presenting AIDS encephalopathy. *Ultrastruct Pathol* 13:433–441.
- Newcombe EA, Camats-Perna J, Silva ML, Valmas N, Huat TJ, Medeiros R (2018) Inflammation: the link between comorbidities, genetics, and Alzheimer's disease. *J Neuroinflammation* 15:276.
- Noda S, Sato S, Fukuda T, Tada N, Hattori N (2020) Aging-related motor function and dopaminergic neuronal loss in C57BL/6 mice. *Mol Brain* 13:46.
- Norden DM, Muccigrosso MM, Godbout JP (2015) Microglial priming and enhanced reactivity to secondary insult in aging, and traumatic CNS injury, and neurodegenerative disease. *Neuropharmacology* 96:29–41.
- O'Koren EG, Yu C, Klingeborn M, Wong AY, Prigge CL, Mathew R, Kalnitsky J, Msallam RA, Silvin A, Kay JN, Bowes Rickman C, Arshavsky VY, Ginhoux F, Merad M, Saban DR (2019) Microglial function is distinct in different anatomical locations during retinal homeostasis and degeneration. *Immunity* 50:723–737.
- O'Neil SM, Witcher KG, McKim DB, Godbout JP (2018) Forced turnover of aged microglia induces an intermediate phenotype but does not rebalance CNS environmental cues driving priming to immune challenge. *Acta Neuropathol Commun* 6:129.
- Orre M, Kamphuis W, Osborn LM, Melief J, Kooijman L, Huitinga I, Klooster J, Bossers K, Hol EM (2014) Acute isolation and transcriptome characterization of cortical astrocytes and microglia from young and aged mice. *Neurobiol Aging* 35:1–14.
- Prieto GA, Cotman CW (2017) Cytokines and cytokine networks target neurons to modulate long-term potentiation. *Cytokine Growth Factor Rev* 34:27–33.
- Primiani CT, Ryan VH, Rao JS, Cam MC, Ahn K, Modi HR, Rapoport SI (2014) Coordinated gene expression of neuroinflammatory and cell signaling markers in dorsolateral prefrontal cortex during human brain development and aging. *PLoS One* 9:e110972.
- Ransohoff RM, Perry VH (2009) Microglial physiology: unique stimuli, specialized responses. *Annu Rev Immunol* 27:119–145.
- Safaiyan S, Besson-Girard S, Kaya T, Cantuti-Castelvetri L, Liu L, Ji H, Schifferer M, Gouna G, Usifo F, Kannaiyan N, Fitzner D, Xiang X, Rossner MJ, Brendel M, Gokce O, Simons M (2021) White matter aging drives microglial diversity. *Neuron* 109:1100–1117.
- Safaiyan S, Kannaiyan N, Snaidero N, Brioschi S, Biber K, Yona S, Edinger AL, Jung S, Rossner MJ, Simons M (2016) Age-related myelin degradation burdens the clearance function of microglia during aging. *Nat Neurosci* 19:995–998.
- Sala Frigerio C, Wolfs L, Fattorelli N, Thrupp N, Voytyuk I, Schmidt I, Mancuso R, Chen WT, Woodbury ME, Srivastava G, Möller T, Hudry E, Das S, Saido T, Karran E, Hyman B, Perry VH, Fiers M, De Strooper B (2019) The major risk factors for Alzheimer's disease: age, sex, and genes modulate the microglia response to A $\beta$  plaques. *Cell Rep* 27:1293–1306.
- Salas IH, Burgado J, Allen NJ (2020) Glia: victims or villains of the aging brain? *Neurobiol Dis* 143:105008.
- Salter MW, Stevens B (2017) Microglia emerge as central players in brain disease. *Nat Med* 23:1018–1027.
- Sarter M, Albin RL, Kucinski A, Lustig C (2014) Where attention falls: increased risk of falls from the converging impact of cortical cholinergic and midbrain dopamine loss on striatal function. *Exp Neurol* 257:120–129.
- Scheiblich H, Dansokho C, Mercan D, Schmidt SV, Bousset L, Wischhof L, Eikens F, Odainic A, Spitzer J, Griep A, Schwartz S, Bano D, Latz E, Melki R, Heneka MT (2021) Microglia jointly degrade fibrillar alpha-synuclein cargo by distribution through tunneling nanotubes. *Cell* 184:5089–5106.
- Shaerzadeh F, Phan L, Miller D, Dacquel M, Hachmeister W, Hansen C, Bechtle A, Tu D, Martcheva M, Foster TC, Kumar A, Streit WJ, Khoshbouei H (2020) Microglia senescence occurs in both substantia nigra and ventral tegmental area. *Glia* 68:2228–2245.
- Sharaf A, Kriegstein K, Spittau B (2013) Distribution of microglia in the postnatal murine nigrostriatal system. *Cell Tissue Res* 351:373–382.
- Shoji H, Takao K, Hattori S, Miyakawa T (2016) Age-related changes in behavior in C57BL/6J mice from young adulthood to middle age. *Mol Brain* 9:11.
- Siddiqi Z, Kemper TL, Killiany R (1999) Age-related neuronal loss from the substantia nigra-pars compacta and ventral tegmental area of the rhesus monkey. *J Neuropathol Exp Neurol* 58:959–971.
- Soto C, Pritzkow S (2018) Protein misfolding, aggregation, and conformational strains in neurodegenerative diseases. *Nat Neurosci* 21:1332–1340.
- Spittau B (2017) Aging microglia-phenotypes, functions and implications for age-related neurodegenerative diseases. *Front Aging Neurosci* 9:194.
- Stephan AH, Kim L, Lovelett EA, Rowitch DH, Barres BA, Berns DS, Tenner AJ, Huang EJ, Madison DV, Coutellier L, Fraser DA, Mateos JM, Tsai HH, Shamloo M (2013) A dramatic increase of C1q protein in the CNS during normal aging. *J Neurosci* 33:13460–13474.
- Stowell RD, Wong EL, Batchelor HN, Mendes MS, Lamantia CE, Whitelaw BS, Majewska AK (2018) Cerebellar microglia are dynamically unique and survey Purkinje neurons in vivo. *Dev Neurobiol* 78:627–644.
- Taetzsch T, Block ML (2013) Pesticides, microglial NOX2, and Parkinson's disease. *J Biochem Mol Toxicol* 27:137–149.
- Tremblay MÈ, Zettel ML, Ison JR, Allen PD, Majewska AK (2012) Effects of aging and sensory loss on glial cells in mouse visual and auditory cortices. *Glia* 60:541–558.
- Vainchtein ID, Molofsky AV (2020) Astrocytes and microglia: in sickness and in health. *Trends Neurosci* 43:144–154.
- VanRyzin JW, Marquardt AE, Argue KJ, Vecchiarelli HA, Ashton SE, Arambula SE, Hill MN, McCarthy MM (2019) Microglial phagocytosis of newborn cells is induced by endocannabinoids and sculpt sex differences in juvenile rat social play. *Neuron* 102:435–449.
- Visser JE, Bloem BR (2005) Role of the basal ganglia in balance control. *Neural Plast* 12:161–174.
- Walker KA, Gottesman RF, Wu A, Knopman DS, Gross AL, Mosley TH, Selvin E, Windham BG (2019) Systemic inflammation during midlife and cognitive change over 20 years: the ARIC Study. *Neurology* 92:e1256–e1267.
- Wolf SA, Boddeke HW, Kettenmann H (2017) Microglia in physiology and disease. *Annu Rev Physiol* 79:619–643.
- Wooten GF, Currie LJ, Bovbjerg VE, Lee JK, Patrie J (2004) Are men at greater risk for Parkinson's disease than women? *J Neurol Neurosurg Psychiatry* 75:637–639.
- Xu H, Ren D (2015) Lysosomal physiology. *Annu Rev Physiol* 77:57–80.